Lithos 352–353 (2020) 105293

Contents lists available at ScienceDirect

Lithos

journal homepage: www.elsevier.com/locate/lithos

Boron isotope composition of coexisting tourmaline and hambergite in alkaline and granitic pegmatites

Øyvind Sunde [a,*], Henrik Friis [a], Tom Andersen [b], Robert B. Trumbull [c], Michael Wiedenbeck [c], Peter Lyckberg [d], Samuele Agostini [e], William H. Casey [f,h], Ping Yu [g]

[a] Natural History Museum, University of Oslo, P.O. Box 1172, Blindern, 0318 Oslo, Norway
[b] Department of Geosciences, University of Oslo, P.O. Box 1047, Blindern, 0316 Oslo, Norway
[c] GFZ German Research Centre for Geosciences Potsdam, Telegrafenberg B125, 14473 Potsdam, Germany
[d] Musée National d'Histoire Naturelle Letzebuerg, 25, rue Münster, L-2160, Luxembourg
[e] Institute of Geosciences and Earth Resources, National Research Council of Italy, Via G. Moruzzi 1, 56124 Pisa, Italy
[f] Department of Earth and Planetary Sciences, University of California, Davis, CA 95616, United States
[g] NMR Facility, University of California, Davis, CA 95616, United States
[h] Department of Chemistry, University of California, Davis, CA 95616, United States

ARTICLE INFO

Article history:
Received 4 June 2019
Received in revised form 13 November 2019
Accepted 14 November 2019
Available online 16 November 2019

Keywords:
Boron isotopes
Pegmatites
Alkaline
Tourmaline
Hambergite

ABSTRACT

The boron isotopic composition of tourmaline and hambergite (Be_2BO_3[OH,F]) from peraluminous ($n = 12$), peralkaline ($n = 1$), and peralkaline nepheline syenite ($n = 16$) pegmatites has been measured by secondary ion mass spectrometry, for which a new hambergite reference material was developed. The focus of this study is on nepheline syenite pegmatites from the Larvik Plutonic Complex (Norway) and one peralkaline pegmatite related to the nearby Eikeren-Skrim Complex (Norway), where we investigate the source of boron as being from magmatic vs. external fluids. Tourmaline-hambergite mineral pairs were also analysed from peraluminous pegmatite localities (Russia, Tajikistan, and Pakistan) to test for systematic B-isotope fractionation between these two minerals.

Tourmaline and hambergite from peraluminous granitic pegmatites have light boron ratios ($\delta^{11}B = -12.9$to -1.0‰) associated with S-type granites, whereas peralkaline granitic and nepheline syenite pegmatites have boron ratios ($\delta^{11}B = -1.7$ to 11.8‰), which we interpret is a result of heavy-boron enrichment from external fluids. Our data show that hambergite tracks isotope variations of its geochemical setting and could therefore be used as a proxy mineral in place of tourmaline when geochemical stability favours hambergite.

The results suggest a slight but consistent partitioning of B-isotopes between tourmaline and hambergite, with $\Delta^{11}B = \delta^{11}B_{tourmaline} - \delta^{11}B_{hambergite}$ in the range of approximately −3‰ to −5‰. Boron is in trigonal coordination with oxygen in both of these mineral phases as verified by NMR. Single crystal XRD analyses of tourmaline and hambergite reveal consistent longer <B-O> distances of tourmaline relative to hambergite. We attribute the boron isotopic fractionation to the longer <B-O> bond-lengths in tourmaline compared with hambergite.

1. Introduction

Boron is a trace element in most igneous rocks, where average concentrations between 2 and 11 μg/g are typical in granites and felsic volcanic rocks (Trumbull and Slack, 2018). However, boron can be enriched in highly-evolved granitic magmas up to weight percent (wt%) concentrations where B-rich minerals may crystallise (e.g., Morgan and London, 1989; Vorbach, 1989). The most common B-rich mineral is tourmaline (general formula $XY_3Z_6[T_6O_{18}][BO_3]_3V_3W$; Henry et al., 2011). Hambergite ($Be_2BO_3[OH,F]$) is much less common, but it occurs in both peraluminous and peralkaline nepheline syenite pegmatites, and may occur with other B-rich minerals such as tourmaline (Brøgger, 1890; Fisher et al., 1998; Thomas and Davidson, 2010; Vladykin and Sotnikova, 2017). Boron is soluble in aqueous fluids and it partitions to aqueous solution, although not strongly, at the magmatic-hydrothermal transition. Boron has two naturally-occurring isotopes (^{10}B and ^{11}B) whose ratio is expressed as permil ($\delta^{11}B$) values relative to NIST SRM-951. The range of $\delta^{11}B$ values in nature is approximately 60‰ (e.g., Marschall and Jiang, 2011). This makes the boron isotope system a valuable tracer of the boron source(s) and their mixing relations in magmatic and hydrothermal systems. However, the application of boron isotopes is complicated by fractionation between melts, minerals and aqueous fluids, and such fractionation depends on temperature, melt and/or fluid composition and on the structural

* Corresponding author.
E-mail address: oyvind.geologi@gmail.com (Ø. Sunde).

https://doi.org/10.1016/j.lithos.2019.105293
0024-4937/

configuration of boron in the phases involved (e.g., Kowalski and Wunder, 2018).

As a small ion (0.01–0.11 Å; Shannon, 1976), B^{3+} enters into both trigonal (III) and tetrahedral (IV) sites in mineral structures, and forms both III- and IV-coordinated oxy-anions in aqueous solutions and silicate melts (Hålenius et al., 2010; Lussier et al., 2009; Schmidt et al., 2005). The coordination environment plays a first-order role in the partitioning of ^{10}B and ^{11}B between two or more phases. Experimental studies of B-isotope fractionation between minerals, melts and fluid exist (Hervig et al., 2002; Kowalski and Wunder, 2018; Maner and London, 2018; Marschall et al., 2009; Meyer et al., 2008; Wunder et al., 2005), but these experiments are conducted for acidic conditions whereas alkaline fluids have neutral to basic pH.

There is now a large amount of published boron isotope data for tourmaline from peraluminous granites and pegmatites (e.g., Maner and London, 2017; Siegel et al., 2016; Trumbull et al., 2013), whereas few $\delta^{11}B$ data are available for tourmaline in alkaline rocks (Bailey, 2006; Kaliwoda et al., 2011). Also, very little is known about the B-isotopic composition of hambergite and virtually nothing is known about the fractionation of boron isotopes between coexisting tourmaline and hambergite. Experiments and computational modelling have shown that ^{10}B and ^{11}B preferentially partition between III- and IV-coordination, respectively (Kowalski and Wunder, 2018 and references therein). Boron occurs dominantly in three-fold coordination as BO_3^{3-} groups in tourmaline and hambergite (Bosi, 2018; Gatta et al., 2012), so a strong isotopic fractionation is not expected. However, tourmaline is known to incorporate some $^{[4]}B$ (e.g., Lussier et al., 2009) and hambergite has two tetrahedral positions normally occupied by Be (*Be1* and *Be2*; Gatta et al., 2012) which can, in principle, also accommodate B^{3+}. Tetrahedral boron could influence the fractionation of boron isotopes between hambergite and tourmaline and should be considered (e.g., Kutzschbach et al., 2017).

In this paper, we explore the B-isotope composition of tourmaline and hambergite in a number of pegmatite settings worldwide to address two distinct research goals: (i) to investigate the origin of boron-rich fluids that precipitate tourmaline and hambergite in peralkaline and nepheline syenite pegmatites of the Larvik Plutonic Complex (LPC) and the nearby Eikeren-Skrim Complex (ESC) in the Oslo Rift of Norway, and (ii) to determine empirical B-isotope fractionation factors between coexisting tourmaline and hambergite in the LPC and in pegmatites from other localities and geochemical environments.

2. Geologic setting of pegmatites and samples used in the study

The pegmatite localities sampled for this study cover a compositional range from peralkaline to peraluminous. The localities include (i): A suite of peralkaline nepheline syenite pegmatites from the Oslo Rift, Norway, (ii): One peralkaline pegmatite in the Oslo Rift, and (iii): Peraluminous pegmatites from Pakistan Himalaya, Central Transbaikalia and Pamir located in the eastern Tajikistan. Our localities and the number of samples are summarised in Table 1 and their geologic settings are briefly described below. Table 2 describes the mineralogy and geologic setting of the tourmaline and hambergite samples used in this study. Fig. 1 shows images of representative specimens from which tourmaline and hambergite were analysed. The samples represent two modes of occurrence; 1) tourmaline and hambergite pairs in direct contact with each other, or within the same, cm-sized sample, and 2) individual tourmaline or hambergite crystals. This is not used to evaluate boron fractionation between tourmaline and hambergite. However, data from this group constrains boron isotopic composition if only one of the two is present.

2.1. Peralkaline nepheline syenite pegmatites, Larvik Plutonic Complex, Oslo Rift, Norway

The Larvik Plutonic Complex (LPC) is a composite intrusion of intermediate monzonitic rocks in the Permo-Carboniferous continental Oslo Rift (Neumann, 1980; Neumann et al., 2004). The LPC comprises approximately 10,000 km^3 of monzonitic rocks and was emplaced between 298 ± 0.4 and 289± 0.5 Ma during the initial opening of the Oslo Rift (Larsen et al., 2008; Neumann et al., 2004; Rämo and Andersen, 2011). The internal structure of the LPC consists of 10 semi-concentric ring sections (Petersen, 1978). According to Neumann (1980), each ring section (RS) represents an individual pluton derived from batches of a common parental magma that fractionated at different crustal levels, where in-situ fractionation of feldspar led to monzonite varieties carrying either quartz (RS 1–2), nepheline (RS 4,6–8), or neither quartz nor nepheline (RS 3 and 5) (Fig.2). Initial whole-rock Sr, Nd, Hf, and Pb isotopic compositions indicate a depleted mantle region as the source of the monzonitic magmas with no significant contamination by crustal components (Neumann et al., 1988; Rämo and Andersen, 2011; Sundvoll et al., 1990).

Thousands of pegmatites are situated in the LPC with the greatest abundance of pegmatites occurring in RS 6 (Sunde et al., 2018). These pegmatites can be classified as either nepheline syenite (agpaitic) or syenite (miaskitic) pegmatites based on their mineral assemblage (e.g., Brøgger, 1890). The nepheline syenite pegmatites typically contain complex mineral assemblages including high-field strength elements, HFSE, (e.g., Zr, Nb, Ti), which crystallised together with the main magmatic mineral assemblages consisting of microcline, nepheline, biotite, magnetite, sodic-calcic and sodic amphibole, and sodic clinopyroxene (aegirine-augite to aegirine) (Piilonen et al., 2013). Late magmatic zeolite-group minerals are common in LPC pegmatites as interstitial masses and replacement products within feldspathoids such as sodalite and nepheline (Brøgger, 1890; Sunde et al., 2019). Analcime, natrolite, gonnardite and thomsonite-Ca are the most common zeolites (e.g., Larsen, 2010) and rare Be-bearing zeolites such as chiavennite have also been reported (e.g., Raade et al., 1983). The late-magmatic assemblages also include sulphide minerals (e.g., molybdenite, chalcopyrite, and pyrite) and Al-hydroxides (e.g., diaspore), which are among the last pegmatite minerals to form.

Table 1
Summary of geological setting of studied pegmatites.

Locality	Tur	Ham	Pegmatite mineralogy	Geological setting
LPC[1,2,3,4]	10	6	Mc, ab, nph, bt, wgm, egm, mt, (anl), (ntr), (fl), (dsp), (chv), (leu), (mz),	Monzonites, nepheline syenite
Malkhan[5,6]	1	1	Qz, K-fsp, tur, lpd, bt, ms, ab, grt, (tur), (qz), (tpz), (brl), (dbr)	Bt-granite and leucogranite
Pakistan[7,8]	3	2	K-fsp, ab, qz, bt, ms, sch, brl, grt, (aq), (clv), (fl), (spd), (lpd), (mrg), (sps), (F-ap),	Leucocratic bt-ms-gneiss and granite
Pamir[9,10]	2	3	Qz, K-fsp, tur, brl, tpz	Bt-granite and leucogranite
ESC[11,12]	1	–	Amz, qz, gad, dan, phe, (tur), (dbr), (nsd), (apy), (py), (cpy),	Alkali granite, marine carbonate

Ab = albite, amz = amazonite, anl = analcime, apy = arsenopyrite, aq = aquamarine, brl = beryl, bt = biotite, chv = chiavennite, clv = cleavelandite, cpy = chalcopyrite, dan = danalite, dbr = danburite, dsp = diaspore, egm = eudialyte group minerals, F-ap = fluorapatite, fl = fluorite, gad = gadolinite, grt = garnet, K-fsp = sodic feldspar, leu = leucophanite, lpd = lepidolite, mc = microcline, mrg = morganite, ms = muscovite, mt = magnetite, mz = monazite, nph = nepheline, nsd = nordenskiöldine, phe = phenakite, py = pyrite, sch = schorl, spd = spodumene, sps = spessartine, tpz = topaz, tur = tourmaline, wgm = wöhlerite group minerals. Minerals in brackets are those occurring in pockets or interstitial. Tur and Ham refer to number of analysed tourmaline and hambergite samples, respectively. Literature data obtained from [1]Brøgger (1890) [2]Neumann (1980), [3]Sunde et al. (2018), [4]Andersen et al. (2010, 2013), [5]Zagorsky and Peretyazhko (2010), [6]Zagorsky (2015), [7]Kazmi et al. (1985), [8]Laurs et al. (1998), [9]Dufour et al. (2007), [10]Pashkov and Dmitriyev (1982), [11]Hansteen and Burke (1995), [12]Sunde (2013).

Table 2
Summary of tourmaline and hambergite samples.

Sample	Locality	Mineral	Setting and accessory minerals
Peralkaline and nepheline syenite pegmatites			
T8	AS Granite*[b]	P Tur	Embedded in zeolite
H1	AS Granite*[b]	P Ham	Embedded in zeolite
T7	AS Granite*[c]	P Tur	Embedded in zeolite
H2	AS Granite*[c]	P Ham	Embedded in zeolite
T4	Klåstad	P Tur	Interstitial masses <5 cm, Figs. 1A
H4†	Klåstad	P Ham	Tabular crystals <2 cm, chv, cc, ms, sch, Fig. 3
T1	Thorstein	S Tur	Single crystal fragment
T2	Rønningen	S Tur	Mc, anl, secondary sdl
T3	Almenningen*	S Tur	Embedded in zeolite
T5	Hjertnesåsen	S Tur	Single crystal fragment
T9	AS Granite*[d]	S Tur	Cavity in altered anl
T10	AS Granite*[d]	S Tur	Mc, anl, ntr, clay, Fig. 1K
TSK1	Skallist	S Tur	Embedded in anl, Fig. 1H
H3†	Tuften* #13458	S Ham	Embedded in anl, Fig. 1B
H5	Bjørndalen* #14341	S Ham	Fl, anl, Fig. 1C
H6	Langangen #43610	S Ham	Embedded in anl, Fig. 1F
T11	ESC	S Tur	Amz, qz, dbr, dan
Peraluminous pegmatites			
H2_TAD1†	Fantaziya	P Ham	Miarole, intergrowths, Fig. 1G
T_TAD1	Fantaziya	P Tur	Miarole, intergrowths, Fig. 1G
H_TAD1	Fantaziya	P Ham	Miarole, intergrowths, Fig. 1G
H_TAD2	Dorozhnaya	P Ham	Miarole, intergrowths, Fig. 1E
T_TAD2	Dorozhnaya	P Tur	Miarole, intergrowths, Fig. 1E
H_RUS2	Orieshnaya	S Ham	Miarole, dbr
T_RUS2	Orieshnaya	S Tur	Miarole, dbr
H_PAK1	Bulachi[a]	P Ham	Miarole, intergrowth, Fig. 1D
T_PAK1	Bulachi[a]	P Tur	Miarole, intergrowth, Fig. 1D
T_PAK2	Bulachi[a]	S Tur	Miarole, lose crystals
T_PAK6	Bulachi[a]	S Tur	Miarole, lose crystals
H_PAK3	Bulachi[a]	S Ham	Miarole, lose crystals

*Tvedalen area, [a]Same miarolitic pocket, [b–d]Denotes different pegmatites within the same quarry, P = pair, S = single, # = NHM collection number, † = samples analysed by MAS NMR.
Mineral abbreviations: Amz = amazonite, anl = analcime, brl = beryl, f-ap = fluorapatite, cc = calcite, chv = chiavennite, dan = danalite, dbr = danburite, fl = fluorite, ham = hambergite, mc = microcline, ms = muscovite, ntr = natrolite, sch = scheelite, sdl = sodalite, spe = spessartine, tur = tourmaline, tpz = topaz, qz = quartz.

Tourmaline is not a common mineral in the LPC nepheline syenite pegmatites, whereas hambergite is more abundant. Sampled hambergite and tourmaline from these pegmatites are not in direct grain-contact, but rather are embedded within the same zeolite hosts. Both minerals crystallised after the primary magmatic stage of pegmatite evolution that involved crystallisation of microcline, nepheline, biotite, sodalite, and albite. Hambergite from LPC pegmatites form elongated tabular euhedral crystals up to 1–2 cm in length. Fig. 3 shows hambergite sample H4 and accessory mineral assemblages occurring within the sample.

2.2. Peralkaline granitic pegmatites, Eikeren-Skrim Complex, Oslo Rift, Norway

Peralkaline granitic rocks in the Eikeren-Skrim Complex (ESC) form the granitic end-member of a series of intermediate (which includes the LPC) and silicic intrusive rocks in the Oslo Rift. Historically, peralkaline granites belonging to the ESC have been referred to as ekerite. The ESC granite is not part of the LPC as it is separated by geography and in time by approximately 18 My with whole-rock Rb—Sr ages of 271 ± 2 Ma (Rasmussen et al., 1988). The ESC granite consists of alkali feldspar, riebeckite and arfvedsonite, sodic amphiboles, and minor biotite. Miarolitic veins and cavities up to 5 cm in size are abundant throughout the ESC. Common minerals in the miaroles include aegirine, alkali amphibole, and halide minerals (Hansteen and Burke, 1995). Several pegmatites form a pegmatite field around the ESC and they are hosted by feldspar-cordierite hornfels of an Ordovician calcareous protolith. Pegmatites in this area primarily consist of microcline, sodic amphibole, clinopyroxene, and minor astrophyllite and helvine. One pegmatite forms a large (< 100 m long) sill intrusion and contains a unique set of minerals that includes tourmaline, amazonite, danburite, danalite, phenakite, and sulphide minerals (Sunde, 2013). This unique mineral assemblage, however, only comprises approximately 16 m of the entire pegmatite where it wedges and terminates into the host rock. Note that this is the only pegmatite of this study that does not contain hambergite.

2.3. Peraluminous granitic pegmatites, Malkhan, Transbaikalia, Russia

The Malkhan complex is located on Malkhan Ridge SE of the Baikal Lake, Transbaikal, Russia. The complex consists of metagabbroids, amphibole-metadiorites, and amphibole-biotite quartz gneissic-granites intruded by the Oreshnyi and Bol'scherechenskii granitic massifs, which are interpreted to be connected at depth and represent the roof facies of a larger underlying pluton (Thomas et al., 2012; Zagorsky, 2015; Zagorsky and Peretyazhko, 2010). Both massifs consist of subalkaline granites and minor calc-alkaline porphyritic biotite granites with local biotite leucogranites at their margin. The vast majority of miarolitic pegmatites are situated between the two massifs (Zagorsky and Peretyazhko, 2010). The ages of pegmatites and granites, determined by ^{40}Ar—^{39}Ar dating, are 124–128 Ma (Zagorsky and Peretyazhko, 2010). The Malkhan granite-pegmatite system is renowned for colourful tourmaline crystals in miarolitic cavities (e.g., Zagorsky, 2015). The sampled Oreshnaya pegmatite is hosted by metagabbroic rocks and metadiorite located close to the Oreshnyi Massif (i.e., Fig. 3 in Zagorsky, 2015).

2.4. Peraluminous granitic pegmatites, Bulachi, Pakistan Himalaya

The sampled pegmatite is located near Bulachi on the south bank of the Indus River, in the Gilgit-Baltistan region of NE Pakistan, which is famous for the occurrence of gem-bearing pegmatites (Kazmi et al., 1985). The pegmatites in this area form swarms of parallel oriented veins emplaced in the Nanga Parbat Haramosh massif (NPHM). The NPHM consists of leucocratic biotite-muscovite gneiss, biotite-gneiss, granite-gneiss, and amphibolite (Kazmi et al., 1985). Laurs et al. (1996, 1998) reported muscovite ^{40}Ar—^{39}Ar ages of <10 Ma from one pegmatite and a granite-gneiss belonging to the NPHM.

2.5. Peraluminous granitic pegmatites, Muzkol Rangkul, Pamir, Tajikistan

Two pegmatites were sampled from the Kukurt area in the Muzkol metamorphic complex (MMC) of Tajikistan: (i) the Fantaziya pegmatite on Tura Kuloma Ridge and (ii) the Dorozhnaya pegmatite on the western valley slope of the Kukurt River. The pegmatites are spatially related to the leucocratic Neogene Shatput granites and emplaced in amphibolite-facies gneisses and schists of the MMC (Dufour et al., 2007; Pashkov and Dmitriyev, 1982).

The Fantaziya pegmatite (Chila Fantaziya) forms a lenticular body that is about 10 m in length with a maximum thickness of 3 m, which is semi-concordant with its marble host rocks. The pegmatite contains abundant schorl and cavities up to 1.5 m^3 consisting of quartz, albite, tourmaline, topaz, fluorite, hambergite, and jeremejevite. Hambergite forms single colourless crystals up to 14 cm in length and 1.5 cm in cross section and as overgrowths on quartz crystals. Hambergite is also contained in quartz as needle-shaped inclusions, and in some cases small tourmaline crystals grow on or out of hambergite crystal faces.

The Dorozhnaya pegmatite is hosted by alternating amphibole-biotite gneisses, quartzite-sandstones, and marbles. The pegmatite has an overall lenticular shape with a nearly vertical dip. It is exposed for a distance of 30 m and has a thickness ranging from 1 m to 10 m. Where the pegmatite swells in thickness it contains miaroles which

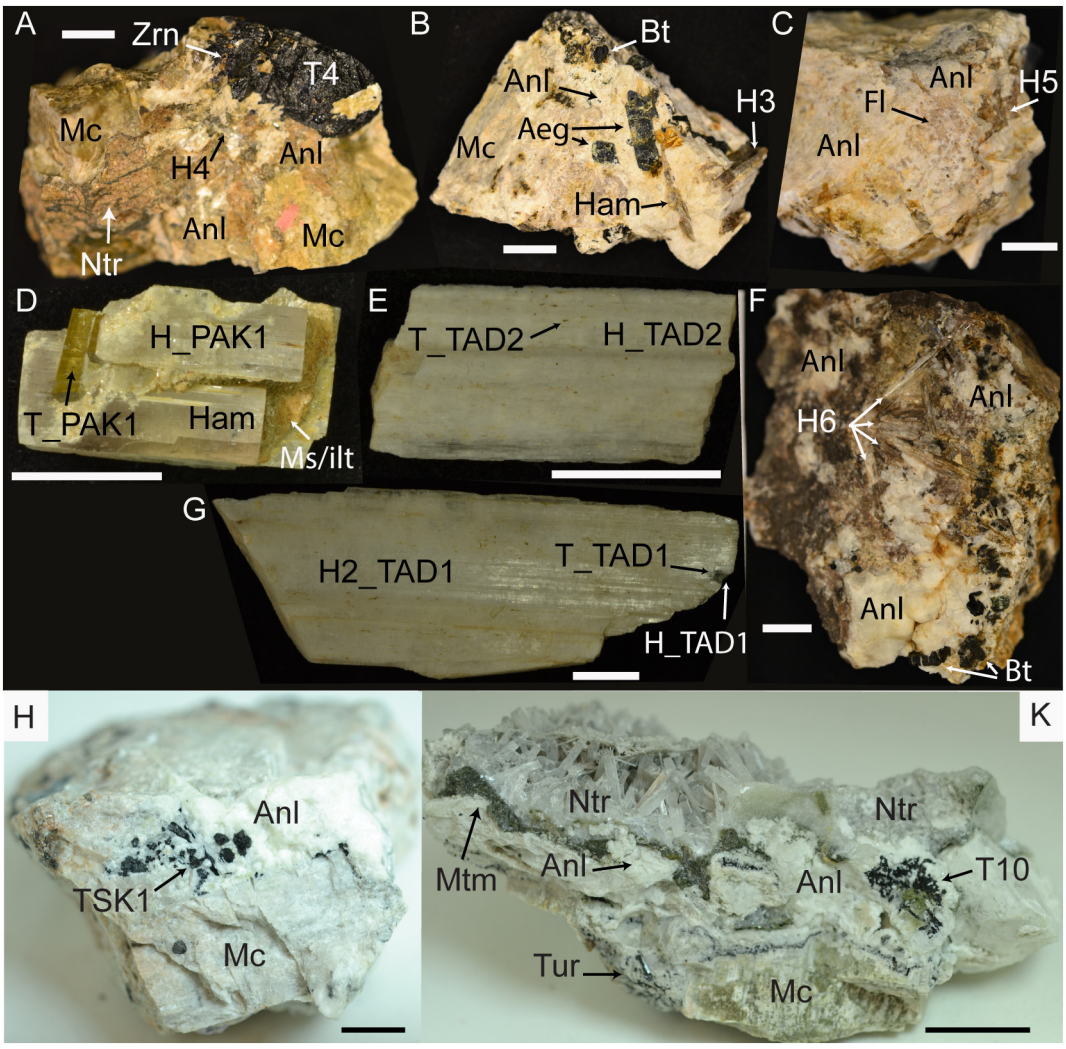

Fig. 1. Photographs of representative samples used in the study. All scales set to 1 cm, mineral abbreviations as follows: Anl = analcime, Aeg = aegirine, Bt = biotite, Fl = fluorite, Ham = hambergite, ilt = illite, Mc = microcline, Mtm = montmorillonite, Ms. = muscovite, Ntr = natrolite, Tur = tourmaline, and Zrn = zircon. Analysed samples labelled in each fig. A: Tourmaline and hambergite (T4 and H4) from the Klåstad quarry. B: Hambergite (H3) from the Tuften quarry, Tvedalen, LPC. C: Hambergite (H5) from the Bjørndalen quarry, Tvedalen, LPC (no tourmaline). D: Tourmaline and hambergite samples (H_PAK1 and T_PAK1) from Bulachi, Pakistan. E: Hambergite (H_TAD2) and tourmaline (T_TAD2), where several small (<2 mm) longtourmalines are embedded on the crystal faces of hambergite H_TAD2, Dorozhnaya pegmatite, Tajikistan F: Radiating tabular hambergite (H6) from Langangen, LPC. G: One hambergite crystal (H2_TAD1) with tourmaline (T_TAD1) embedded on the crystal tip. Hambergite (H_TAD1) was removed from the tip of tourmaline T_TAD1 (indicated by arrow). H: Tourmaline TSK1 embedded in analcime, Skallist quarry, LPC. Analcime and tourmaline are interstitial to primary microcline. I: Tourmaline T10 embedded in analcime. Between the analcime and natrolite zeolites is a small wedge of fine grained montmorillonite clay. This zeolite assemblage is typical for closed pockets in LPC pegmatites.

are partly or completely filled with white clay and tabular fragments of K-feldspar. Some miaroles are 1 m^3 or larger and contain loose crystals of tabular cleavelandite, quartz, K-feldspar, tourmaline, hambergite, and danburite.

3. Analytical methods

3.1. Electron probe microanalysis (EPMA)

All samples were mounted in epoxy, polished and carbon coated to investigate growth zonation using a scanning electron microscope (SEM) prior to further analyses. Semi-quantitative analyses and backscattered electron (BSE) images were collected on a Hitachi S-3600 N scanning electron microscope fitted with a Bruker XFlash 5030 detector at the Natural History Museum, University of Oslo. Based on the SEM BSE imaging and energy dispersive spectrum (EDS) measurements, three epoxy mounts were prepared for EPMA and SIMS boron isotope analysis. Tourmaline reference materials (Table 3) were added to the sample mounts along with the unknown samples.

Quantitative major element contents of tourmaline were determined with a Cameca SX100 electron probe micro analyser (EPMA) at the Department of Geosciences, University of Oslo. The following natural and synthetic standards were used for calibration: Wollastonite (Ca Kα, Si Kα), albite (Na Kα), orthoclase (K Kα), pyrophanite (Mn Kα, Ti Kα), Fe-metal (Fe Kα), synthetic Cr_2O_3 (Cr Kα), synthetic MgO (Mg Kα), synthetic corundum (Al Kα), and fluorite (F Kα). Intensity data were corrected for both inter-element overlaps, and for matrix effects using the PAP procedure (Pouchou and Pichoir, 1984). Fluorine content was not measured on LPC tourmaline. Calculations of tourmaline structural formula were normalised to 31 anions where the B_2O_3, H_2O, and Li_2O content were calculated based on stoichiometry after Clark (2007). The latter was iterated by adding Li_2O until cations at the *Y*, *Z*, and *T* sites summed up to 15 apfu and neutral charge balance was maintained.

The major element composition of hambergite was not measured by EPMA because the mineral consists of Be, B, H, and O, most of which cannot be measured using an EPMA. To determine the concentration of fluorine in hambergite we used a trace-matrix setup assuming a bulk composition corresponding to the ideal formula of pure OH end-member $Be_2BO_3(OH)$. Atomic proportions were set to

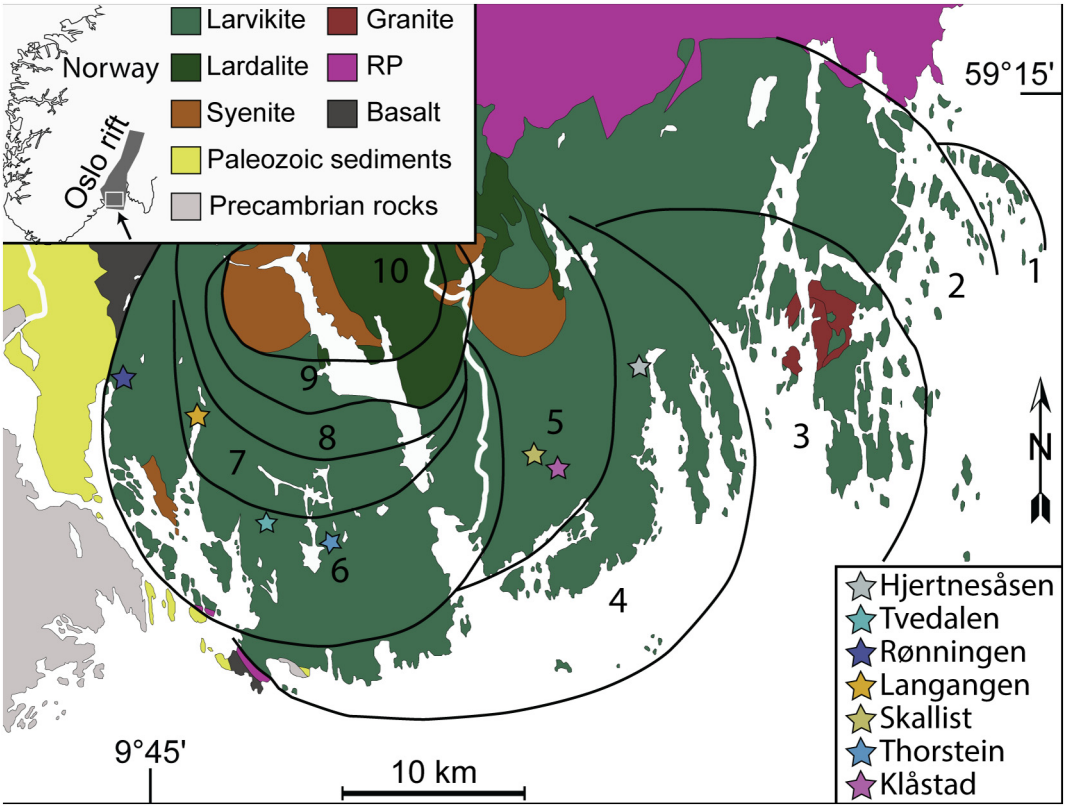

Fig. 2. Simplified geological map of the LPC modified from Petersen (1978) and Lutro and Nordgulen (2008). Numbers 1–10 represents RS number. Inset map shows location of the Oslo Rift in the Scandinavian Peninsula and arrow indicates enlarged detailed area. Stars indicate sampled areas referred to in the text, where Tveidalen includes the following localities: Bjørndalen, AS Granite, Almenningen, and Tuften. Geographical coordinates according to the WGS84 geodetic datum.

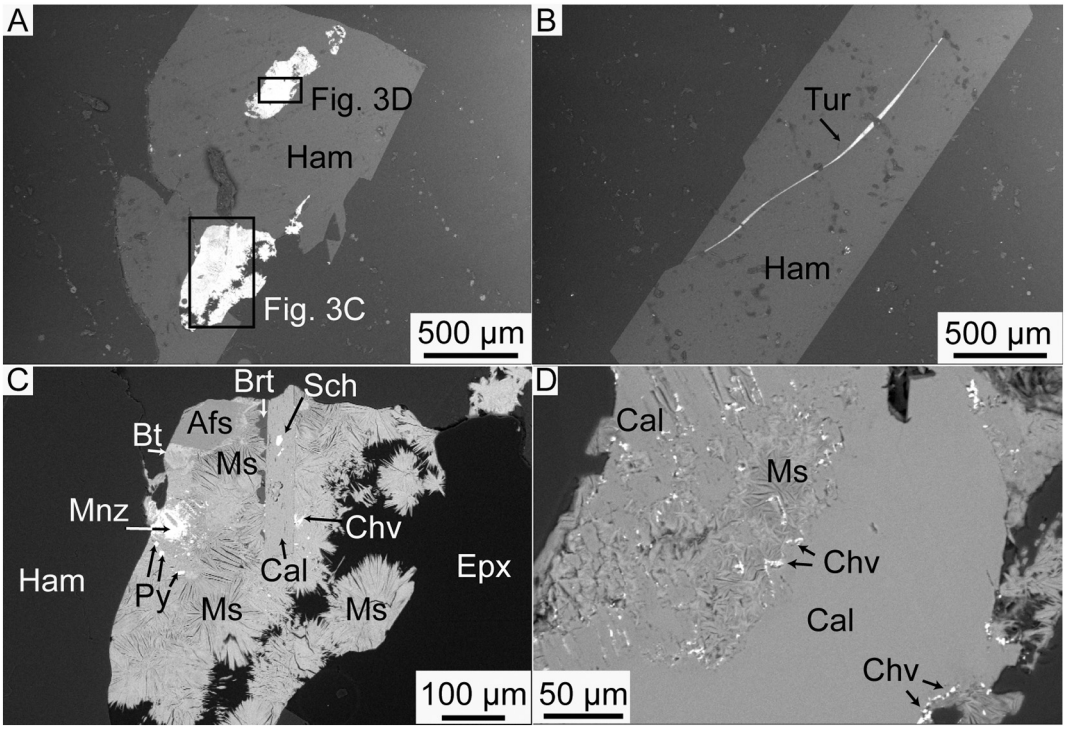

Fig. 3. Backscattered electron images of hambergite (H4). A: Hambergite with alteration zones (boxes show areas for C, D). B: Hambergite (ham) with tourmaline (tur) filling a fracture. C: Close-up BSE image of alteration zone within one fragment of sample H4. Afs = alkali feldspar, sch = scheelite, chv = chiavenite, ms = muscovite, bt = biotite, mnz = monazite, py = pyrite, hmb = hambergite, brt = bertrandite, cal = calcite, epx = epoxy. Afs crystal shows an alteration rim with a mix of biotite and muscovite. North-south oriented elongated calcite crystal is enclosed by muscovite and minor chiavenite along the calcite – muscovite rim. Embedded within the calcite is a small anhedral scheelite crystal, and bertrandite (brt) interstitial to calcite and muscovite. D: Enlarged view of alteration zone in hambergite H4. Minor chiavenite (chv) mantle the grain boundary between muscovite (ms) and calcite (cal) shown as bright BSE spots.

Table 3
Summary of SIMS B-isotope analyses of reference materials.

Analysis date	$^{11}B/^{10}B$[a]	StDev[b]	IMF[c]	$\delta^{11}B$(‰)[d]	Rep. (‰)[e]	*n*
Schorl ($^{11}B/^{10}B$ = 3.9931 and $\delta^{11}B$ = −12.5‰)						
05.03.2018	3.9090	<0.001	0.9789	−12.0	0.17	11
09.10.2018	3.9062	0.002	0.9782	−12	0.52	13
Dravite ($^{11}B/^{10}B$ = 4.0169 and $\delta^{11}B$ = −6.6 ‰)						
05.03.2018	3.9285	<0.001	0.9780	−7.1	0.12	11
09.10.2018	3.9254	0.002	0.9772	−7.1	0.67	15
Mean IMF (schorl + dravite)						
05.03.2018			0.9784		0.51	22
09.10.2018			0.9777		0.79	28
Elbaite ($^{11}B/^{10}B$ = 4.0014 and $\delta^{11}B$ = −10.4‰)						
09.10.2018	3.9000	0.002	0.9746	−10.4	0.53	15
Hambergite ($^{11}B/^{10}B$ = 3.9938 and $\delta^{11}B$ = −12.3 ‰)						
08.10.2018	3.9766	0.002	0.9956	−12.3	0.73	34
09.10.2018	3.9879	0.004	0.9985	−12.2	1.02	14

Schorl, dravite, elbaite are reference tourmalines 112,566, 108,796 and 98,144, respectively (Leeman and Tonarini, 2001); Hambergite is an in-house reference material developed for this study.

[a] Mean measured $^{11}B/^{10}B$ ratio of "*n*" analyses.
[b] 1σ standard deviation of measured $^{11}B/^{10}B$ ratios of "*n*" analyses.
[c] Instrumental mass fractionation factors; the mean (schorl+dravite) IMF was used to correct tourmalines of schorlitic-dravitic composition and the elbaite IMF was used to correct elbaitic tourmalines (see text).
[d] Relative to $^{11}B/^{10}B$ = 4.04362 for NBS SRM 951.
[e] Repeatability based on "*n*" analyses (standard deviation/mean) * 1000.

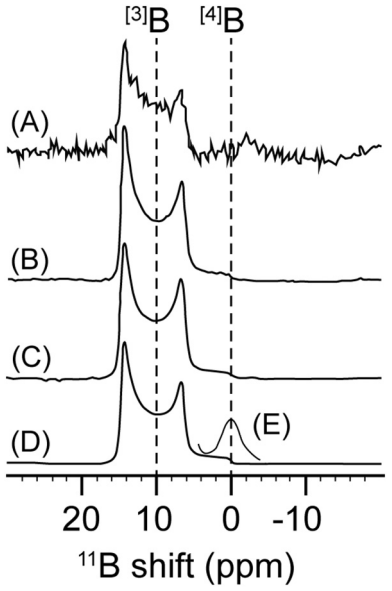

Fig. 4. Hambergite MAS NMR results. Chemical shift of ^{11}B in hambergite samples H3 (A), H4 (B), H2_TAD1 (C), and the hambergite reference sample (HII) (D). Note that limited material of sample H4 yielded shorter runtime. Reference data for $^{[4]}B$ in danburite (E), and theoretical chemical shifts of $^{[3]}B$ and $^{[4]}B$ indicated by dashed lines (Kirkpatrick et al., 1985; Turner et al., 1986).

Be = 19.2, B = 11.5, and O = 68, summing up to a theoretical total value of 98.9 wt%.

3.2. Nuclear magnetic resonance and single-crystal X-ray diffraction

Magic-angle spinning (MAS) nuclear magnetic resonance (NMR) experiments were conducted on four hambergite samples (H3, H4, H2_TAD1, and boron isotope reference sample HII) using a Bruker AVANCE 500WB spectrometer equipped with a 11.74 Tesla Bruker magnet at the NMR Facility, University of Davis. Hambergite samples were ground with an agate mortar and pestle, and packed into a 4-mm zirconia rotor with a Kel-F cap. A direct polarization single pulse sequence was used for ^{11}B NMR data acquisition, and Larmor frequency was 160.455 MHz. The ^{11}B MAS NMR data were collected with a 1 μs (i.e., 22.5° tip angle) pulse and 30 s of relaxation delay. The NMR signals were accumulated by 16 to 2100 scans for signal averaging. Due to the limited amount of material for sample H4 (Fig. 4A), the number of scans were 2100 and lasted for 17.5 h. Chemical shifts were externally referenced to Be_2SiO_4 and 0.1 M $Na_2B_4O_7$ solution to 0 ppm and 9.8 ppm, respectively. Relaxation delay time for ^{11}B NMR was measured using a saturation-recovery pulse sequence consisting of eight 90° train with a 100 ms inter-pulse delay.

Single-crystal X-ray diffraction intensity data were collected for 12 hambergite and 17 tourmaline crystals at the Natural History Museum in Oslo using a Rigaku Synergy-S diffractometer equipped with a HyPix-6000HE detector. A PhotonJet-S microfocused sealed tube operated at 50 kV and 1 mA providing Mo*K*α radiation. The structures were solved by direct methods (Sheldrick, 2008) using neutral atom scattering factors. After all non-hydrogen atoms were located, anisotropic displacement factors were applied and the structures refined with SHELXL (Sheldrick, 2015).

3.3. Boron isotope analyses

The boron isotopic composition of tourmaline and hambergite were measured by MC-SIMS using a CAMECA 1280-HR mass spectrometer at the GeoForschungs-Zentrum (GFZ) Potsdam. The sample mounts were re-polished to remove their carbon coat, ultrasonically cleaned with ethanol, and then sputter coated which deposited a 35 nm thick, high purity gold layer. Analyses were conducted with a 13 kV, 0.8 nA $^{16}O^-$ primary beam focused to a 5 μm diameter spot on the sample surface. A 5 min pre-burn was used to remove the gold coat and to attain steady state sputtering conditions in the analytical region. The instrument was operated at mass resolving power (M/ΔM) approximately 1900, which is more than sufficient to resolve the isobaric interference of $^{10}B^1H$ and $^9Be^1H$ on masses ^{11}B and ^{10}B, respectively. Instrumental mass fractionation (IMF) and analytical quality were monitored by multiple measurements on the reference tourmalines schorl, dravite, and elbaite described by Leeman and Tonarini (2001). The Potsdam SIMS lab has determined a slight but significant chemical matrix effect between schorl-dravite tourmalines and tourmalines of elbaite compositions (ca. 2‰, see Kutzschbach et al., 2017). Thus, we took care to use matrix-matched reference tourmalines for correction of the unknown tourmaline samples. For schorlitic compositions typical of the LPC we used the average of all schorl and dravite IMF factors combined, whereas elbaitic samples were corrected for IMF using the factor determined on the elbaite reference material. Table 3 gives a summary of standard reference material used and the instrumental mass fractionation corrections. Internal precision for individual analyses was less than ±0.3‰ at 1σ for the 20 integration steps. Standard mean error of all measurements for combined schorl-dravite and for elbaite reference samples at 1σ were ca. ±0.8‰ and 0.5‰, respectively (Table 3). The final $\delta^{11}B_{tourmaline}$ values were calculated relative to NIST SRM 951 using $^{11}B/^{10}B$ = 4.04362 from Catanzaro et al. (1970).

For the hambergite analyses it was necessary to prepare an in-house reference material, which is stored at GFZ, Potsdam. We chose to use a hambergite sample (HII) from the Bulachi pegmatite, Pakistan, taken from the same miarolitic pocket as sample H_PAK3 (Table 2). Multiple SIMS analyses (n = 34) of three grains showed the sample to be isotopically homogeneous e.g., standard deviation of all measured $^{11}B/^{10}B$ ratios were <0.002 at 1σ. The material was analysed for its boron isotopic composition at the Institute of Geosciences and Earth Resources IGG in Pisa (Italy) using a Neptune plus multi-collector inductively coupled plasma mass spectrometer (MC-ICPMS). A representative aliquot of sample HII was crushed then melted in a platinum crucible along with purified K_2CO_3. Boron was extracted by adding B-free water and then split into two batches where the first batch was processed according to Tonarini et al. (1997) in a three-stage setup. The second batch was

processed by diluting the solution with 2% HNO_3 without any further chemical separation. Both batches produced similar results with $\delta^{11}B = -12.38$ and -12.22, respectively ($n = 6$). All samples were diluted to 15–25 ng/g B and run in 10 blocks each consisting of six cycles. Measurements were conducted with sample and standard bracketing, and blank corrected in a series of successions. The NBS 951 and B4 IAEA IGG reference materials were processed in the same session to determine accuracy and precision for the procedure. The $^{11}B/^{10}B$ ratio, as determined by MC-ICPMS, of the hambergite reference material is 3.99388 and this value was used to determine IMF values for SIMS analyses. Final $\delta^{11}B_{hambergite}$ values were calculated relative to NIST SRM 951 using the $^{11}B/^{10}B$ value of 4.04362 from Catanzaro et al. (1970). The average $\delta^{11}B$ of 48 SIMS analyses of the reference hambergite gave −12.3‰, which is consistent with the wet-chemical determination. Internal precision for individual analyses were less than ±0.2‰ at 1σ for the 20 integration steps. Standard mean error at 1σ for all measurements of the hambergite reference material was ca. ±0.73‰ and ± 1.01‰ for two separate sessions (Table 3).

4. Results

4.1. Hambergite boron coordination and fluorine variations

Spectra of ^{11}B MAS NMR are similar for all four samples (Fig. 4). The ^{11}B MAS NMR spectra for all samples consist of a second-order quadruple pattern with only one ^{11}B site in the crystalline structure. The isotropic chemical shift is at 17.02 ppm consistent with triangular coordinated B. Triangular boron gives a broad quadrupole-split peak from about +9 to +17 ppm B, whereas the strong $^{[4]}B$ peak expected at 1.5 ppm (Fig. 4E) is absent (Hålenius et al., 2010; Turner et al., 1986). Therefore, all analysed samples show only triangular boron. Furthermore, SXRD results show no anomalous short Be—O bond-lengths, which would have been the case if B entered the tetrahedral position in hambergite.

Table 4 shows measured fluorine content in hambergite samples from peralkaline nepheline syenite and peraluminous granitic pegmatites. Fluorine varies between 0.3 ± 0.1 and 7.0 ± 0.08 wt% F in H5 and H2_TAD1, respectively. Hambergite from LPC nepheline syenite pegmatites are relatively fluorine-poor with the highest recorded F content in sample H1 with 1.3 ± 0.1 wt% F. Comparatively, hambergite from peraluminous granitic pegmatites are relatively fluorine-rich with the majority of samples containing >1.5 wt% F (Table 4). Sample H2_TAD1 has two domains, H2_TAD1 bright and H2_TAD1 dark (Table 4), with 3.3 and 7.0 wt% F, respectively. This zonation in respect to F variation appeared to be small-scale slightly bright or dark BSE areas. A clear and widespread crystal zonation was not recognised, but we infer there is a discrete fluorine variation in H2_TAD1 reflected by the high standard deviation (Table 4).

Table 4
Results of hambergite fluorine analyses by EPMA.

Sample	*n*	F wt%[a]
Peralkaline nepheline syenite		
H1	5	1.3 (1)
H2	6	0.8 (1)
H3	15	0.5 (3)
H4	14	0.6 (2)
H5	12	0.3 (1)
H6	7	0.5 (2)
Peraluminous		
H2_TAD1 bright	3	3.3 (8)
H2_TAD1 dark	3	7.04 (6)
H2_TAD1	5	5 (2)
H_TAD1	8	1.5 (1)
H_TAD2	7	3.4 (8)
H_PAK1	5	1.56 (7)
H_PAK3 bright	5	5.5 (1)
H_PAK3 dark	3	3.81 (7)
H_RUS2	9	0.73 (3)

[a] Mean value from "*n*" measurements, parenthesis indicates 2 standard deviation of "*n*" analyses, "dark" and "bright" refer to BSE images (see text).

4.2. Tourmaline major element composition

Tourmaline crystals from peraluminous pegmatites were too large (> thin-section size) to investigate whole-crystal zonation patterns, but the fragments mounted in epoxy did not reveal significant zonation. Table 5 lists major element composition of all tourmaline samples. All analysed LPC tourmalines have high Fe/(Fe + Mg) ratios and classify as schorlitic tourmaline in the alkali group (Figs. 5 and 6) according to a third level hierarchal approach after Henry et al. (2011). The contents (in atoms per formula unit or apfu) of Na, (Fe + Mg), and Al in LPC schorlitic tourmalines suggest full occupancy of the *X, Y, Z*- sites, respectively. This is in agreement with previously measured schorl compositions and single crystal X-ray diffraction by Kolitsch et al. (2013) on samples from the same localities of T3 and T7-T10. Sample TSK1 record the highest Al and lowest Fe contents with 7.11 and 1.27 apfu, respectively. Thus, TSK1 is the only measured LPC tourmaline with excess Al with respect to the *Z*-site. However, this sample sum up to a relatively low total sum (98.31), and contain excess Al (1.1 apfu) in the *Y*-site, which may indicate a minor Li component. The highest Na and Mg contents were found in samples T1 and T3 with 1.0 and 0.9 apfu, respectively. Iron (assumed divalent) reached the highest content in T7 with 2.9 apfu. Calcium and potassium contents were negligible with (Ca + K) < 0.02 apfu, while Cr was below detection limit and thus omitted from Table 5. Peraluminous tourmaline samples are rich in Al with 7.5–8.0 apfu, but have low contents of Na and Fe with 0.6 and < 0.1 apfu, respectively. Lithium was not quantitatively determined, but the Li_2O content was calculated according to stoichiometry and neutral charge balance. Samples T_RUS2, T_TAD1, T_TAD2, T_PAK1, and T_PAK6 are treated as elbaitic tourmaline based on the apfu contents of Fe, Mg, and inferred Li (Figs. 5 and 6). Fluorine contents were measured for the peraluminous tourmalines where the highest F content is in sample T_PAK6 with 0.82 apfu, while the lowest values are in T_PAK2 and T_RUS2 with 0.27 and 0.31 apfu, respectively. Iron content in all measured tourmalines is treated as divalent, however nepheline syenite pegmatites contain abundant aegirine and there may be minor trivalent iron present.

4.3. Tourmaline and hambergite boron isotope composition

Table 6 presents average $\delta^{11}B$ ratios for all measured tourmaline and hambergite samples. Tourmaline and hambergite from nepheline syenite pegmatites yielded average $\delta^{11}B$ values from −1.7(3) ‰ (T1) to 4.0(6) ‰ (T9) and 2(1) ‰ (H4) to 9.9(1) ‰ (H5), respectively. The B-isotope ratios of both minerals in the peraluminous pegmatites are more variable with a total range between −1.0(1) ‰ (H_TAD1) and −12.9(7) ‰ (T_PAK1). The $\delta^{11}B$ range for all tourmaline samples is between −12.9(7) ‰ (T_PAK1) and 11.8(4) ‰ (T11). Hambergite from peraluminous pegmatites vary between −12.3(7) ‰ (HII) and −1.0(1) ‰ (H_TAD1). The large range of $\delta^{11}B$ values for all tourmaline and hambergite samples is expected and is a result of comparing pegmatites with different petrogenetic histories. Tourmaline and hambergite fragments were measured with a minimum of 5 analytical points, and several samples were represented by multiple fragments. Measured fragments were internally homogenous with the exception of tourmaline sample T8 that yielded higher standard deviation due to $\delta^{11}B$ varying between −0.9‰ and 1.1‰ with average $\delta^{11}B$ of 0(1) (Table 6).

Fig. 7 shows that in most cases, the B-isotope ratio of hambergite is higher than the related tourmaline by approximately 3‰. Exceptions are samples H4 and H_PAK1, where the hambergite is still heavier than the associated tourmaline, but by 1 and 8‰, respectively. Hambergite samples H_TAD1 and H2_TAD1 represent two separate

Table 5
Results of tourmaline analyses by EPMA.

	T1	T2	T3	T4	T5	T7	T8	T9	T10
n	8	8	10	9	10	11	10	10	11
Wt%[b]	Sch	Sch	Sch	Sch	Sch	Sch	Sch	Sch	Sch
SiO_2	34.8 (1)	34.2 (6)	35.0 (3)	34.3 (3)	34.5 (2)	34.5 (3)	34.7 (4)	34.4 (6)	34.8 (3)
Na_2O	2.96 (7)	2.90 (7)	2.9 (1)	2.9 (1)	2.87 (5)	2.89 (9)	2.93 (8)	2.94 (9)	2.89 (8)
K_2O	0.05 (1)	0.05 (2)	0.04 (1)	0.06 (1)	0.04 (1)	0.04 (2)	0.05 (3)	0.05 (1)	0.03 (1)
FeO	19.0 (2)	19 (2)	11.8 (2)	15.8 (2)	20 (1)	20.3 (9)	17.6 (9)	17 (1)	18.5 (5)
MnO	0.14 (3)	0.31 (8)	0.4 (1)	0.94 (7)	0.20 (5)	0.30 (8)	0.9 (3)	0.2 (1)	0.25 (4)
Al_2O_3	28.3 (2)	28 (3)	31.1 (2)	30.9 (2)	28 (1)	27.9 (6)	29.3 (5)	30 (1)	30.2 (5)
MgO	0.52 (7)	0.3 (3)	3.9 (1)	0.94 (4)	0.03 (4)	0.37 (5)	0.5 (2)	0.4 (3)	0.30 (5)
TiO_2	1.27 (7)	0.6 (7)	0.38 (4)	0.52 (6)	0.00 (2)	0.5 (1)	0.2 (1)	0.1 (2)	0.10 (7)
CaO	0	0	0	0.07 (3)	0	0	0	0	0
B_2O_3[a]	10.05	9.96	10.25	10.1	9.95	9.94	10	10.07	10.1
H_2O[a]	3.46	3.44	3.54	3.49	3.43	3.42	3.45	3.48	3.48
Li_2O	–	–	–	–	–	–	–	–	–
F	–	–	–	–	–	–	–	–	–
O=F	–	–	–	–	–	–	–	–	–
Total	100.55	98.76	99.32	100.02	99.03	100.16	99.64	98.64	100.65
apfu									
X-site									
Na^+	1.00	0.98	0.97	0.98	0.97	0.98	0.99	0.98	0.97
K^+	0.01	0.01	0.01	0.01	0.01	0.01	0.01	0.01	0.01
Ca^{2+}	0	0	0	0.01	0	0	0	0	0
Σ*X*	1.01	0.99	0.98	1.0	0.98	0.99	1.0	0.99	0.98
Y-site									
Al^{3+}	0	0	0.21	0.27	0	0	0	0.26	0.13
Fe^{2+}	2.75	2.88	1.68	2.28	2.97	2.86	2.56	2.54	2.67
Mg^{2+}	0.14	0.10	0.98	0.24	0.01	0.10	0.15	0.12	0.08
Mn^{2+}	0.02	0.05	0.07	0.14	0.03	0.05	0.14	0.03	0.04
Li^+	0	0	0	0	0	0	0	0	0
Σ*Y*	2.91	2.98	2.95	2.93	3.01	3.00	2.85	2.95	2.93
Z-site									
Al	5.79	5.90	6.0	6.0	5.96	5.76	6.00	6.0	6.0
Ti	0.17	0.09	0.05	0.07	0	0.07	0.04	0.02	0.01
Fe	0	0	0	0	0	0.12			
Σ*Z*	5.96	5.99	6.05	6.07	5.96	5.95	6.04	6.02	6.01
T-site									
Si	6.03	5.97	5.93	5.90	6.03	6.05	6.03	5.94	6.00
Al	0	0	0	0	0	0	0	0	0
Σ*T*	6.03	5.97	5.93	5.90	6.03	6.05	6.03	5.94	6.00
V + *W*-site									
OH	4.00	4.00	4.00	4.00	3.99	3.99	4.00	4.00	4.00
F	–	–	–	–	–	–	–	–	–
Σ*V* + *W*	4.0	4.0	4.0	4.0	4.0	4.0	4.0	4.0	4.0
B	3.00	3.00	3.00	2.99	3.00	3.00	3.00	3.00	3.00

	TSK1	T_RUS2	T_TAD1	T_TAD2	T_PAK1	T_PAK2	T_PAK6	T11
n	10	10	14	9	9	8	11	10
Wt%[b]	Sch	Elb	Elb	Elb	Elb	Sch	Elb	Sch
SiO_2	36.0 (3)	38 (1)	38.1 (5)	37.6 (2)	37.7 (3)	35.0 (2)	37.1 (3)	34.7 (4)
Na_2O	3.0 (1)	2.1 (4)	1.9 (9)	2.1 (1)	2.2 (1)	1.67 (9)	2.66 (7)	2.4 (1)
K_2O	0.02 (2)	0.01 (1)	0.01 (1)	0.01 (1)	0.02 (1)	0.05 (1)	0.03 (1)	0.07 (1)
FeO	9.1 (8)	0.06 (3)	1.2 (2)	0.21 (3)	0.27 (5)	14.1 (1)	0.6 (1)	17.2 (2)
MnO	0.4 (1)	0.4 (1)	0.12 (6)	1.2 (2)	3.9 (1)	0.41 (8)	6.6 (1)	0.16 (4)
Al_2O_3	36.2 (3)	41.6 (5)	40.4 (3)	40.7 (3)	38.6 (2)	34.2 (4)	37.3 (3)	27.2 (2)
MgO	0	0	0	0	0	0.35 (3)	0	2.4 (1)
TiO_2	0.11 (3)	0.03 (4)	0	0.05 (2)	0.33 (7)	0.6 (1)	0.29 (6)	1.3 (7)
CaO	0	0.3 (4)	1.15 (9)	0.5 (1)	0.91 (8)	0.13 (2)	0.33 (5)	0.65 (5)
B_2O_3[a]	10.45	11.10	11.09	11.00	10.95	10.35	10.82	10.00
H_2O[a]	3.61	3.55	3.25	3.32	3.16	3.33	3.03	3.45
Li_2O[a]	–	2.10	2.19	2.03	1.98	–	1.57	–
F	–	0.6 (3)	1.2 (2)	1.0 (2)	1.3 (2)	0.5 (1)	1.5 (2)	–
O=F	–	0.25	0.51	0.51	0.55	0.21	0.63	–
Total	98.89	99.60	100.11	99.30	100.77	100.48	101.20	99.94
apfu								
X-site								
Na	0.98	0.64	0.58	0.64	0.68	0.54	0.83	0.83
K	0.01	0	0	0	0	0.01	0.01	0.02
Ca	0	0.05	0.19	0.08	0.15	0.02	0.06	0.12
Σ*X*	0.99	0.69	0.77	0.72	0.83	0.57	0.90	0.97
Y-site								
Al	1.11	1.67	1.47	1.58	1.21	0.77	1.05	0
Fe	1.27	0.01	0.16	0.03	0.04	1.98	0.08	2.34
Mg	0	0	0	0	0	0.09	0	0.63

Table 5 (*continued*)

	TSK1	T_RUS2	T_TAD1	T_TAD2	T_PAK1	T_PAK2	T_PAK6	T11
Mn	0.06	0.05	0.02	0.16	0.52	0.06	0.90	0.02
Li	0	1.32	1.38	1.29	1.26	0	1.01	0
ΣY	2.44	3.05	3.03	3.07	3.07	2.98	3.07	3.17
Z-site								
Al	6.0	6.0	6.0	6.0	6.0	6.0	6.0	5.58
Ti	0.01	0	0	0.01	0.04	0.08	0.03	0.18
Fe	0	0	0	0	0	0	0	0.17
ΣZ	6.01	6.00	6.00	6.01	6.04	6.08	6.03	5.93
T-site								
Si	5.99	5.95	5.98	5.94	5.97	5.88	5.95	6.03
Al	0	0.05	0.03	0.06	0.03	0	0.05	0
ΣT	6.0	6.0	6.01	6.0	6.0	5.88	6.0	6.03
$V + W$-site								
OH	4.00	3.71	3.40	3.50	3.34	3.73	3.24	4.00
F	–	0.30	0.60	0.50	0.65	0.27	0.76	–
$\Sigma V + W$	4.0	4.01	4.0	4.0	3.99	4.0	4.0	4.0
B	3.00	3.00	3.00	3.00	2.99	3.00	3.00	3.00

[a] Calculated based on stoichiometry.
[b] Average values, Elb = elbaitic, Sch = schorlitic, parenthesis indicates 2σ standard deviation.

hambergite samples where both are in grain-contact with tourmaline (T_TAD1) (Fig. 1G). These hambergite samples have slightly different B-isotope compositions where H2_TAD1 yielded $\delta^{11}B = -2 \pm 1‰$ and H_TAD1–1.0 ± 0.1‰, whereas the corresponding tourmaline sample T_TAD1 yielded $\delta^{11}B = -6.0 \pm 0.1‰$. Although both hambergite samples show slightly different boron ratios their total $\delta^{11}B$ values form a continuous range, i.e., H_TAD1 from −0.9 to −1.3‰ and H2_TAD1 from −1.3 to −3.2‰. The difference of $\delta^{11}B$ between hambergite (H_TAD1 and H2_TAD1) and tourmaline (T_TAD1) is between 3‰ and 5‰.

5. Discussion

5.1. Conditions of tourmaline and hambergite crystallisation

Boron is an incompatible element in major rock-forming minerals of granitic and monzonitic rocks. Therefore boron preferentially partitions into the residual liquid and becomes enriched in pegmatite-forming melts, and eventually in aqueous fluid. Peretyazhko et al. (2004) and Thomas et al. (2012) showed that melt-inclusions in quartz from Malkhan pegmatites contained up to 10% (g/g) B_2O_3. In a pegmatite-forming melt tourmaline (or other borosilicates) may crystallise directly from the melt if boron is sufficiently enriched and other essential elements are present (e.g., Be for hambergite). Experimental studies have shown that tourmaline crystallise in silicate melts ($T < 700$ °C) or precipitate from a hydrothermal fluid when B_2O_3 concentrations are approximately 2–3 and 0.5–1.0 wt%, respectively (London, 2011; Wolf and London, 1997 and references therein). These experiments have also shown that tourmaline only precipitates from aqueous fluids with acidic to near-neutral pH irrespective of boron concentrations, and that its stability is enhanced by a high alumina saturation index (ASI = molar [Al/(Na + K)] > 1) (London, 2011). For instance, synthetic tourmalines only precipitate in fluids of pH ≤ 7 with high Al_2O_3 components buffered by other peraluminous minerals present in the system (London, 2011; Morgan and London, 1989). These chemical constraints may explain why tourmaline is less abundant than hambergite in the LPC nepheline syenite pegmatites, and rare in low-ASI peralkaline and alkaline rocks in general. Hambergite, as shown by the localities studied here (Table 2), forms in both alkaline and peraluminous pegmatites, however little is known about its stability in various geochemical systems. Thomas and Davidson (2010) reported hambergite melt and fluid inclusions in morganite crystals from the Muiane pegmatite in Mozambique. Their study reported trapping temperatures of 610 °C and 277 °C for hambergite melt and fluid inclusions, respectively. At temperatures above 650 °C and 2 kbar pressure hambergite converts to bromellite (BeO) (Thomas and Davidson, 2010).

Khomyakov (1995) suggested that strongly alkaline pegmatites in general develop through three stages, which is related to changes in alkalinity and mineral assemblages (i.e., successive stages of mineral formation in agpaitic pegmatites). Stage one represents an increase of alkalinity by progressive crystallisation of primary feldspar and feldspathoids along the wall zone (e.g., analogous to graphic granite and blocky feldspar in granitic pegmatites). Stage two is marked by peak alkaline conditions with a maximum level of supersaturation of alkali elements, volatiles and rare metals. Upon cooling, stage three represents a relative decrease in alkalinity, but increase in water activity of the melt and the concentration of dissolved acidic complexes increase, causing zeolite formation and precipitation of Li, Be, and B minerals. Alteration of niobo- and zirconosilicates and precipitation of rare-earth minerals are associated with stage three (Khomyakov, 1995). Markl and Baumgartner (2002) showed that hydrous alteration of feldspathoids in sodalite-foyaites in the Ilímaussaq complex (e.g., analcime replacement of sodalite) was induced by saline fluids with pH around 8–9. Similar mineral replacements of feldspathoids occur in LPC nepheline syenite pegmatites, but this alteration process is generally earlier than zeolite crystallisation and is related to peak alkalinity conditions during pegmatite crystallisation. The fact that tourmaline is found with zeolites in the LPC suggests that the late fluids were of lower pH as suggested by stage three of Khomyakov (1995). Note that the discovery of hexaniobate-minerals in LPC pegmatites indicates that basic fluids prevailed at temperatures < ~50 °C (Friis and Casey, 2018). There is, however, no evidence that tourmaline has crystallised together with the hexaniobate minerals.

Crystallisation temperatures for LPC hambergite and tourmaline have not been constrained, but an upper limit can be inferred from coexisting mineral assemblages. For LPC tourmalines, with or without hambergite, the association with zeolite minerals provides an upper temperature limit around 500 °C. Experimental P-T relations of analcime, natrolite, ± quartz in the system Na_2O – Al_2O3 – SiO_2 – H_2O (e.g., Liou, 1971; Liou et al., 1991) show that analcime dehydrates at $T > 450$ °C with low $aSiO_2$ and moderate fluid-P (> 3 kb) (Liou, 1971). Tourmaline (T11) in the ESC pegmatite form masses interstitial to amazonite. Experiments by Hofmeister and Rossman (1985) showed that amazonite loses its colour when heated above 500 °C, and this is irreversible upon cooling and therefore suggests an upper temperature limit for tourmaline sample T11.

5.2. Boron isotope partitioning between hambergite and tourmaline

Our tourmaline and hambergite $\delta^{11}B$ data show that hambergite consistently has higher/heavier values than tourmaline (Fig. 7). Despite different localities and geologic setting the $\delta^{11}B$ of hambergite is heavier

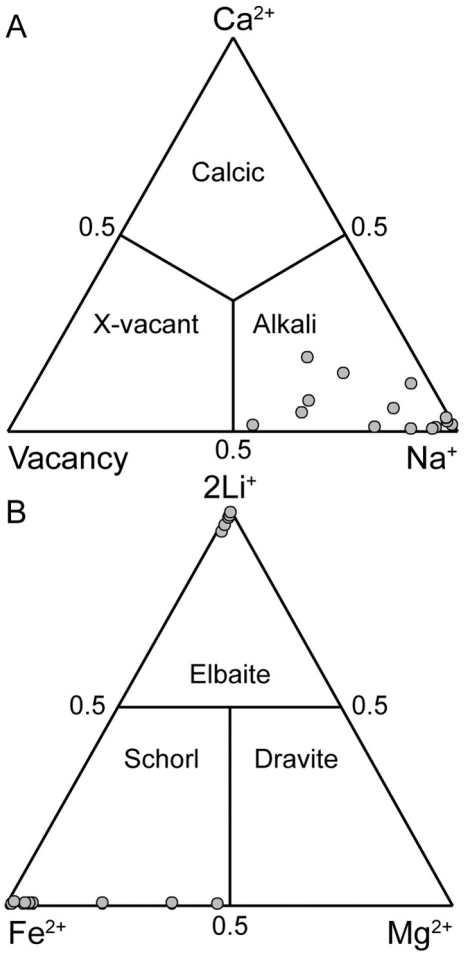

Fig. 5. Ternary plots of 17 tourmaline samples and their *X*-site composition according to nomenclature by Henry et al. (2011). Numbers refer to atoms per formula unit. A) Position of tourmaline samples among the primary tourmaline groups in the system Ca-vacancy-(Na + K). B) Tourmaline composition within the alkali sub-group (note elbaite and schorl are two subgroups).

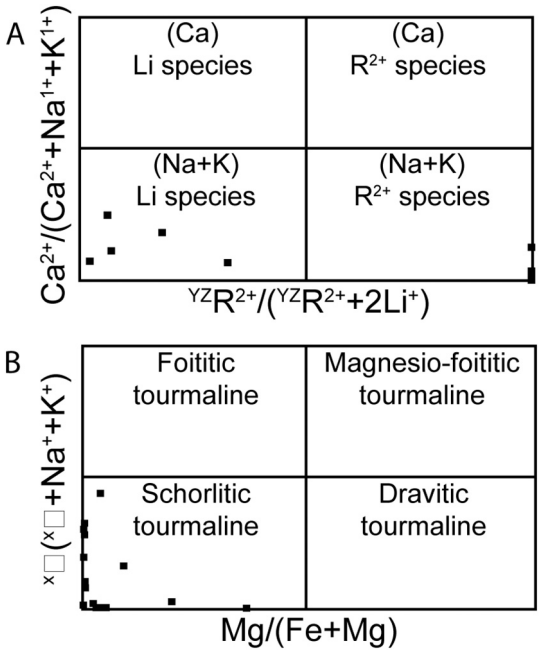

Fig. 6. Tourmaline composition in the alkali subgroups (all plots after Henry et al., 2011) A) Determination of subgroups for alkali-group tourmalines based on the parameters X site = Na + K dominant, Z site = Al dominant, and W site = inferred (OH + F) dominance. Li species belong to alkali-subgroup 2 and (Na + K) species belong to alkali-subgroup 1. B) Diagram of generalised tourmaline species according to the parameters Mg/(Mg + Fe) versus X-site vacancy and (Na + K) ratios.

than tourmaline by 1‰ (T4 + H4) and 8‰ (T_PAK1 + H_PAK1), however most mineral pairs have an approximately 3‰ difference, which suggests it may represent equilibrium partitioning. We rule out the possibility that tourmaline crystallised earlier than hambergite and thereby depleted the pegmatite melt/fluid in ^{10}B before hambergite formed. This scenario would not produce a near-constant shift in $\delta^{11}B$ between the two minerals in separate pegmatites as was observed. The relation between tourmaline and hambergite in the mineral pairs TAD1, TAD2, and PAK1 (Fig. 1), shows that tourmaline is a minor phase relative to hambergite. Furthermore, tourmaline T_TAD2 grew as small crystals on the crystal faces of hambergite sample H_TAD2, which may indicate that tourmaline crystallised after hambergite. Particularly for LPC nepheline syenite pegmatites tourmaline is a minor phase relative to hambergite and both minerals are constrained to the last stage of pegmatite formation.

Tourmaline and hambergite from peralkaline nepheline syenite pegmatites are not in direct contact, but they show the same systematic difference of about 3‰ as in the peraluminous pegmatites. Therefore, it seems that hambergite has heavier boron ratios relative to tourmaline independent of crystallisation sequence and geological setting. The boron isotopic composition of neither hambergite nor tourmaline changes whether the other is present or not (Fig. 7). There are very few studies to compare our results with. Maner and London (2017) reported $\delta^{11}B$ ratios of tourmaline and hambergite from a miarolitic pocket in the Main Dike, Little Three group, California, with mean $\delta^{11}B$ values of 1.0‰ and 20.9 ± 2‰, respectively. In this example hambergite

Table 6
Average tourmaline and hambergite $\delta^{11}B$ values.

Sample/locality	$\delta^{11}B$ (‰)[a]	*n*	1 s.d (‰)[b]	Mineral
Peralkaline and nepheline syenite pegmatites				
T1/Tvedalen	−1.7 (3)	7	0.08	Schorlitic
T2/Rønningen	1.4 (6)	7	0.07	Schorlitic
T3/Tvedalen	0.8 (4)	7	0.08	Schorlitic
T4/Klåstad	0.9 (3)	6	0.08	Schorlitic
T5/Hjertnesåsen	1.6 (9)	7	0.08	Schorlitic
T7/Tvedalen	0.1 (3)	6	0.07	Schorlitic
T8/Tvedalen	0 (1)	6	0.08	Schorlitic
T9/Tvedalen	4.0 (6)	8	0.08	Schorlitic
T10/Tvedalen	0.5 (3)	8	0.08	Schorlitic
TSK1/Skallist	2.2 (5)	9	0.08	Schorlitic
H1/Tvedalen	3 (1)	10	0.10	Hambergite
H2/Tvedalen	3 (1)	11	0.10	Hambergite
H3/Tvedalen	5.9 (2)	10	0.11	Hambergite
H4/Klåstad	2 (1)	13	0.13	Hambergite
H5/Tvedalen	9.9 (1)	10	0.14	Hambergite
H6/Langangen	8.1 (1)	15	0.16	Hambergite
T11/ESC	11.8 (4)	8	0.09	Schorlitic
Peraluminous pegmatites				
T_RUS2/Orieshnaya	−8.4 (8)	10	0.23	Elbaitic
T_TAD1/Fantaziya	−6.0 (6)	10	0.18	Elbaitic
T_TAD2/Dorozhnaya	−4.5 (7)	10	0.27	Elbaitic
T_PAK1/Bulachi	−12.9 (7)	5	0.16	Elbaitic
T_PAK2/Bulachi	−12.0 (3)	5	0.15	Elbaitic
T_PAK6/Bulachi	−12 (1)	10	0.16	Schorlitic
H2_TAD1/Fantaziya	−2 (1)	10	0.11	Hambergite
H_TAD1/Fantaziya	−1.0 (1)	10	0.12	Hambergite
H_TAD2/Dorozhnaya	−1.6 (7)	15	0.13	Hambergite
H_PAK1/Bulachi	−4.8 (3)	5	0.14	Hambergite
H_PAK3/Bulachi	−10 (2)	5	0.19	Hambergite
H_RUS2/Orieshnaya	−3.7 (4)	10	0.16	Hambergite

[a] Average of «*n*» analyses.
[b] Average internal precision from 20 cycles per analyses, parenthesis indicates 2σ standard deviation of "*n*" $\delta^{11}B$ values.

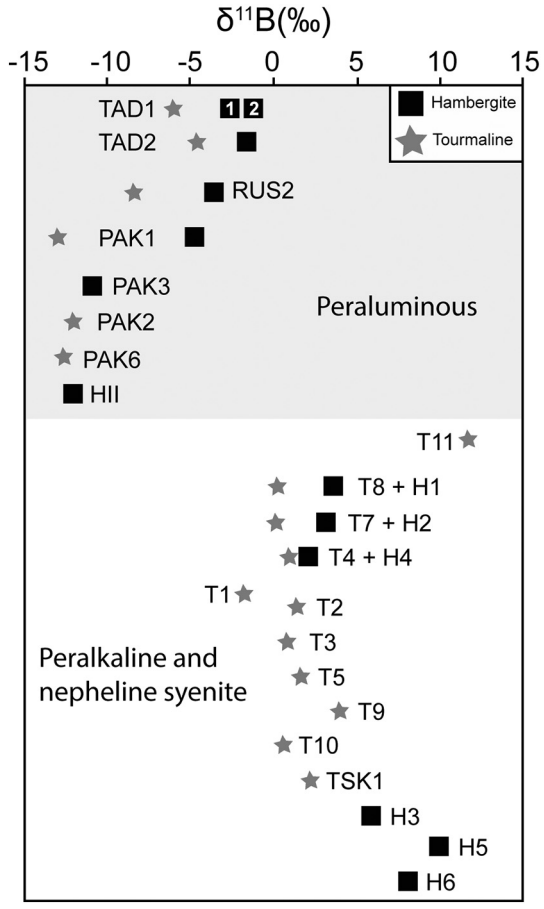

Fig. 7. Overview of $\delta^{11}B$ values of tourmaline-hambergite pairs and unpaired samples by localities. Symbols are larger than the 2σ standard deviation of $\delta^{11}B$. Juxtaposed symbols indicate tourmaline and hambergite pairs. Un-paired samples include PAK 3, PAK 6, RUS 2, HII (hambergite reference materialT1, T2, T3, T5, T9, T10, TSK1, H3, H5, H6, T11). Note hambergite from TAD1 consist of two hambergite samples indicated by numbers 1 and 2 (Fig. 1G).

is isotopically heavier than tourmaline as in our study, but by a much greater amount. However, the authors suggested that the hambergite results may be biased by their use of dravite as a reference material for the SIMS analysis. The data from our study can be used to test this by comparing the hambergite $\delta^{11}B$ values calculated from the dravite and from the hambergite reference materials. For the example, LPC samples H1 and H5 yield $\delta^{11}B$ values of 21 and 27‰ when calculated with a dravite standard, respectively. The difference between dravite-corrected and hambergite-corrected $\delta^{11}B$ values on all LPC hambergite samples yields an average 17.6‰ error. If we take that as a valid estimate of the matrix effect, we estimate that the true value for hambergite from the Little Three Main Dike would be close to ~3‰ and thus consistent with our findings. Pezzotta et al. (2010) determined B-isotope values of coexisting tourmaline, danburite, and hambergite from pegmatites in Central Madagascar. That study did not specify the reference materials used for SIMS IMF correction, but the results showed essentially no difference in the $\delta^{11}B$ values of tourmaline and hambergite (6.2‰–7.3‰ and 7.0‰ for tourmaline and hambergite, respectively.

In summary, there is a slight but systematic difference in B-isotope composition of coexisting tourmaline and hambergite. Boron is nominally in trigonal configuration in both minerals, although tourmaline can contain some tetrahedral boron (< 1 apfu) substituting for Si in the *T*-site (e.g., Lussier et al., 2009). If tourmaline contains tetrahedral boron it will potentially incorporate more ^{10}B relative to hambergite. However, tourmaline with tetrahedral boron is rare in nature and the major-element analyses of our tourmaline samples suggest that the *T*-site is fully occupied by Si (Table 5) and tetrahedral B is insignificant. Furthermore, our structure solutions showed no indication that B enters the tetrahedral Be-site in any of the hambergite samples. A more likely explanation for the tourmaline-hambergite partitioning is a difference in the <B-O > bond-lengths. We collected crystallographic data from all tourmaline and hambergite samples and compare <B-O > distances in Fig. 8. Fig. 8 reveals that hambergite <B-O > vary between 1.3727 and 1.3742 ($n = 12$) Å and average < B-O > of 1.3735(9), whereas tourmaline <B-O > varies between 1. 373–1.379 Å ($n = 17$) with an average of 1.376(3) Å. We do not see a systematic difference in the average < B-O > distances between elbaitic and schorlitic tourmalines in our study. Although Fig. 8 shows three tourmaline samples with shorter or similar <B-O > distances relative to hambergite, these samples are not from the same geochemical system. However, it is clear that the boron coordination in hambergite is generally smaller than in tourmaline and that some overlap between the <B-O > distances exists. In addition, the distortion of the B-coordination (longest bond minus shortest bond) is larger for the tourmalines (0.01(1) Å) compared to that of the hambergites (0.002(1) Å). Therefore there are significant bond-length differences and distortion between BO_3 groups of hambergite and those in tourmaline, where the latter on average has longer B—O bonds relative to hambergite. Since the lighter boron isotope partitions to species with longer, weaker bonds (Kowalski and Wunder, 2018), we interpret that this possibly explains the consistent heavy boron isotope composition of hambergite relative to tourmaline. The importance of not only bond distances, but also the distortion of the B-site for fractionation of B-isotopes is well-known for such similar mineral pairs as calcite and aragonite (e.g., Balan et al., 2018).

5.3. Boron isotope diversity and source implications

Fig. 9 underscores the systematically higher range of $\delta^{11}B$ values for tourmaline and/or hambergite from peralkaline (i.e., peralkaline and peralkaline nepheline syenite) settings in the Oslo Rift (−2 to 12‰) compared to peraluminous Malkhan, Pamir, and Himalayan pegmatites (−13 to −1‰). Fig. 9 compares these two groups of $\delta^{11}B$ ratios (white boxes) with published data from other studies and with various natural source reservoirs for boron. The $\delta^{11}B$ range for Malkhan, Pamir, and Himalayan samples is similar to that for the peraluminous Varuträsk and Borborema pegmatites and with the range of global S-type granites (-11 ± 4‰, $n = 179$) (Trumbull and Slack, 2018). It is reasonable to assume a crustal source for boron in these examples, agreeing with suggested magma genesis by partial melting of a pelitic protolith (Laurs et al., 1998, for the Pakistan Himalaya, and Zagorsky, 2015, for Malkhan).

In contrast, the $\delta^{11}B$ values for the LPC and ESC samples are significantly higher than the crustal range and that of MORB and the depleted mantle (Fig. 9), from which the LPC magmas are thought to have formed (e.g., Neumann, 1980). However, it must be noted that the tourmaline and hambergite in LPC alkaline pegmatites are not primary magmatic, but formed in zeolite-bearing pockets at temperatures below 500 °C. Fractionation of boron isotopes between mineral and melt ($\Delta^{11}B_{melt\text{-}crystal}$) is currently poorly constrained and remains to be determined by experimental studies. As discussed below the magnitude of B isotope fractionation is influenced by temperature and the coordination of boron in melt and solid phase. Experiments of $\Delta^{11}B_{melt\text{-}vapor}$ show that boron isotope fractionation between melt and aqueous fluid is small at high temperatures (e.g., 800 °C), but the magnitude increase at lower temperatures below liquidus (Hervig et al., 2002; Maner and London, 2018). Thus we must consider the possible effects of fluid exsolution from the LPC magma and fluid-mediated crystallisation at sub-magmatic temperature. Only tourmaline is relevant to this discussion because fluid-melt-mineral fractionation factors for hambergite are unknown.

Meyer et al. (2008) determined boron isotopic fractionation between tourmaline and acid-to-neutral aqueous fluids in which boron is trigonally coordinated. Under these conditions the $\Delta^{11}B_{tour\text{-}fluid}$ is

−2.7‰ at 400 °C and −1.9‰ at 500 °C. According to these data the mineralising fluids for LPC and ESC tourmalines had $\delta^{11}B$ values in the range of about 0‰–7‰ and 14–15‰, respectively. If the hydrothermal fluid were considerably more basic such that the dominant B-species in solution is $B(OH)_4^-$ (Schmidt et al., 2005), then the B-isotope partitioning between fluid and tourmaline would be reversed, i.e., with ^{10}B preferring the fluid phase. However, a high pH of the late-stage fluids is unlikely because the studies on tourmaline stability mentioned earlier suggest that tourmaline would not crystallise. Thus, it is likely that the fluids from which tourmaline formed had positive $\delta^{11}B$ values. If one assumes that those fluids were derived from the LPC magma by exsolution, the B-isotope composition of the magma might be estimated. However, the fluid-melt fractionation depends on the contrast in boron coordination between both phases and that cannot reliably be predicted for the melt phase. Whereas $^{[III]}B$ dominates in peraluminous, hydrous granitic melts (e.g., Tonarini et al., 2003) this may not be true for the peralkaline magmas of the LPC.

Previous work on boro-silicate glasses has shown that the addition of alkalis favours conversion of $^{[III]}B$ to $^{[IV]}B$, while addition of aluminum suppresses the formation of $^{[IV]}B$ due to alkali-aluminum complexation (e.g., Geisinger et al., 1988; Wu and Stebbins, 2009, 2013). Thus, a mixed $^{[III]}B$ and $^{[IV]}B$ coordination in the LPC magmas is likely, but at the high temperatures involved, it is unlikely that melt-fluid fractionation can produce a fluid with positive $\delta^{11}B$ from a mantle-derived magma given the MORB composition of $\delta^{11}B = -7$ (Marschall, 2018). Maner and London (2017) also found $\delta^{11}B$ values for tourmaline from the Little Three pegmatites, California, which overlaps with the LPC (Fig. 9). The Little Three pegmatites are associated with I-type (and possibly S-type) plutons of the California coast range and the high $\delta^{11}B$ values relative to MORB were suggested to reflect seawater-altered oceanic crust in the source of those magmas. Altered oceanic crust is an expected component of I-type magmas at subduction margins, and there are many examples of positive $\delta^{11}B$ values in rocks from these settings (Trumbull and Slack, 2018). However, the setting of the Oslo Rift is different and alternative explanations for the heavy isotopic signature of boron are discussed in the next section.

5.4. Boron isotopic composition of Oslo Rift magmas

In principle the heavy isotope signature of tourmaline and hambergite from the LPC and ESC pegmatites may relate to an isotopically-heavy source magma, and/or from an isotopic fractionation between the minerals and magma or fluid from which they crystallised, and/or to an influx of heavy boron from outside the pegmatite system. With reference to the source magma, we can consider three theoretical scenarios by which heavy boron can be introduced into the magmatic system prior to pegmatite formation: (i) boron uptake from the melt source, (ii) boron fractionation within the magma due to crystallisation of solid phases, and (iii) influx of external boron before segregation of the pegmatite-forming magma. Below we evaluate if heavy boron ratios obtained from the LPC and ESC Oslo Rift samples are results of equilibrium isotopic fractionation in the source magma.

Studies of petrogenesis for the LPC suggest that the parental magmas were mantle-derived. The geodynamic setting of the Permian intracontinental Oslo Rift argues against the idea that altered oceanic crust was an important component of the mantle source. Indeed, the intitial Sr, Nd, Hf, and Pb isotopic compositions indicate a depleted mantle source for the precursor to the monzonitic magmas, without significant contamination by crustal components (Neumann et al., 1988; Rämo and Andersen, 2011; Sundvoll et al., 1990). Therefore it is justified

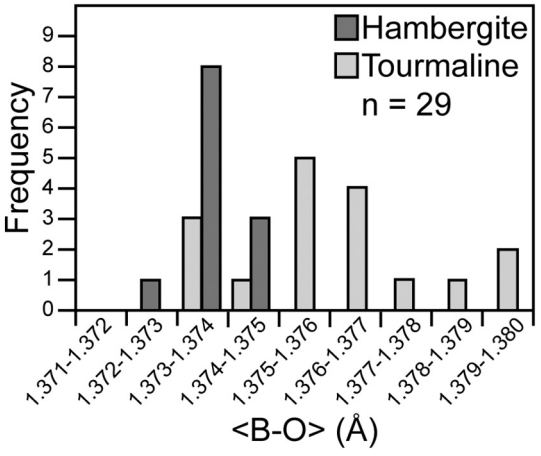

Fig. 8. Plot of <B-O > bond-length frequency for tourmaline and hambergite samples used in the study. Hambergite <B-O > bond-lengths are between 1.372 and 1.375 Å with the highest frequency ($n = 8$) in the 1.373–1.374 Å range. Tourmaline have longer <B-O > bond-lengths relative to the associated hambergite sample, and the highest <B-O > frequency occur in the range of 1.375–1.376 Å ($n = 5$). Note that some tourmaline samples have shorter <B-O > bonds than hambergite, however these tourmaline and hambergite samples are not related by locality.

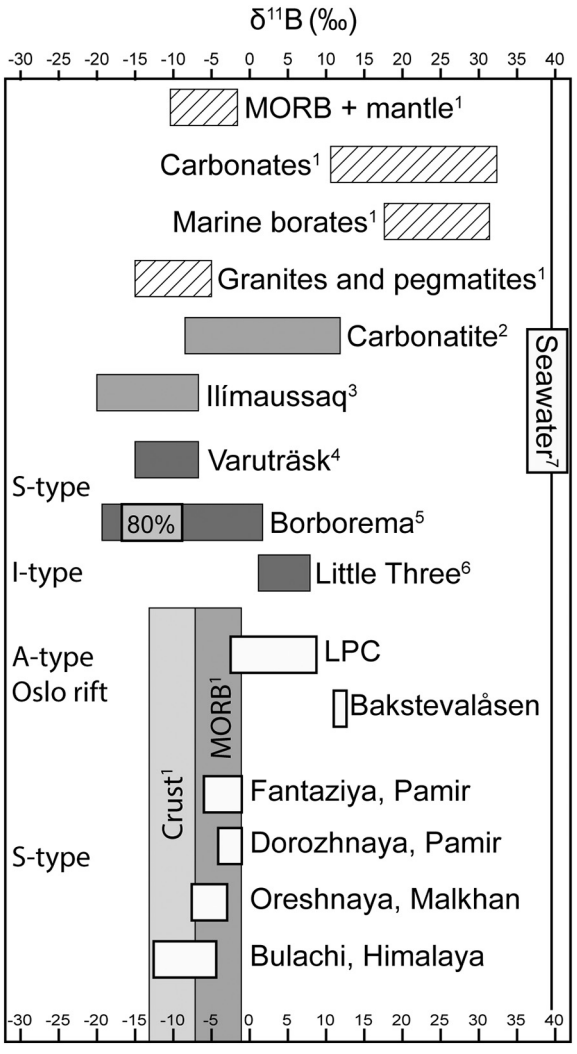

Fig. 9. $\delta^{11}B$ ranges of tourmaline and hambergite from pegmatites, tourmaline in felsic rocks and terrestrial boron reservoirs. Diagonal lines = B reservoirs; grey = literature data; white = this study; columns = $\delta^{11}B$ of average crust and unaltered MORB. Data for LPC and Bakstevalåsen are related to peralkaline A-type magmatism, whereas the other pegmatite data are related to metaluminous and peraluminous magmas. Literature data from [1]Van Hinsberg et al. (2011), [2]Çimen et al. (2018), [3]Kaliwoda et al. (2011), [4]Siegel et al. (2016), [5]Trumbull et al. (2013), [6]Maner and London (2017), and [7]Foster et al. (2010). Note that Borborema pegmatites cover a wide range, whereas the main (80%) $\delta^{11}B$ data are between −17 and −9 ‰ (Trumbull et al., 2013).

to suppose a MORB-like B-isotope composition of the LPC parental magma, i.e., $\delta^{11}B = -7 \pm 1‰$ (Marschall, 2018).

Fractional crystallisation of minerals that selectively incorporate ^{10}B from the parental magma could in theory shift the isotope ratio of a residual melt to higher values. However, there are no abundant, early-formed B-minerals in the LPC monzonites, nor yet in the pegmatites. Hålenius et al. (2010) reported that boron can substitute for silicon in clinopyroxene through an exchange mechanism between SiO_4 and BO_3 groups. Extended fractional crystallisation of pyroxene from the LPC monzonites might be postulated to fractionate boron and its isotopes, between source pluton and residual melt. This, however, is unlikely given the large modal amount of pyroxene required, and also pyroxene would need to have a selective uptake of ^{10}B relative to the magma, i.e., incorporate boron in tetrahedral coordination. However, this is unlikely as the experiments by Hålenius et al. (2010) showed that synthetic clinopyroxene contained boron as BO_3 units, and therefore little isotope fractionation can be expected.

External boron with a heavy isotopic composition relative to MORB-like boron signatures can potentially be introduced to pegmatite-forming magmas, and thereby lead to heavy boron ratios as recorded by the Oslo Rift tourmaline and hambergite samples. Metamorphic fluids derived from contact metamorphism of sediments surrounding the LPC and ESC therefore remain as a plausible scenario and is discussed below.

5.5. Source of heavy boron in LPC nepheline syenite pegmatites

Primary boron minerals as major constituents are not known from LPC pegmatites. Oftedal (1964) reported elevated boron concentrations up to 0.5 wt% in meliphanite and mosandrite from pegmatites closest to the western LPC contact in the Langesundsfjord area (Fig. 2). Among the common primary minerals of LPC nepheline syenite pegmatites, sodalite and amphibole are the only ones which are even moderately compatible with boron (see Kaliwoda et al., 2011 for sodalite partition coefficients). However, these minerals are not modally abundant to change the boron isotope composition of the pegmatite magma. Furthermore, primary sodalite show extensive in-situ alteration by metasomatic fluids, which would cause remobilisation of light boron sequestered in that phase (e.g., Sunde et al., 2019). Therefore, the remaining hypothesis to explain the high $\delta^{11}B$ values is that heavy boron was sourced externally as outlined above.

The authors propose that external boron has been introduced by fluids derived from thermal metamorphism of Paleozoic sediments, which host both the LPC and ESC as contact metamorphosed hornfels. Studies of contact metamorphism in the Oslo Rift have shown that decarbonation reactions and devolatilization of the Paleozoic shale-limestone successions at different areas were controlled by external C-poor and H_2O-rich fluids (Jamtveit et al., 1991, 1997). Along the SW area of the Oslo Rift (i.e., close to the LPC), metamorphism of the Paleozoic succession was mainly governed by an increased permeability by devolatilization reactions and migration of meteoric fluids (Jamtveit et al., 1991).

Oftedal (1964) speculated that elevated boron content recorded in meliphanite from LPC nepheline syenite pegmatites was related to their close proximity to this hornfels. He also observed that leucophanite in pegmatites further away from the contact contained no boron. The timing of precipitation of tourmaline and hambergite in the LPC pegmatites is constrained to the late-magmatic phase of pegmatite formation where they crystallised in late pockets with zeolite minerals. These mineral assemblages are clearly subsolidus phases that formed at temperatures lower than 500 °C (see above), and there is no evidence in the field that hydrothermal veins cross-cut the pegmatites. Therefore we propose that the timing of external boron being introduced to the pegmatite-forming melt was early and prior to final consolidation of the pegmatites.

Çimen et al. (2018) investigated boron isotopic composition of carbonatites from the Miaoya complex in central China, and found that these rocks had heavy boron ratios related to hydrothermal fluids. Light boron ratios ($\delta^{11}B$ of −7‰) were interpreted as the boron isotope signature sourced from the upper mantle, whereas heavy boron ratios, $\delta^{11}B$ up to 12‰, were caused by external hydrothermal fluids. Although these data are valid for carbonatite rocks and not tourmaline or hambergite minerals, the study of Çimen et al. (2018) shows that external fluids may discretely influence boron ratios. We therefore evaluate an external boron source as a likely scenario for the heavy $\delta^{11}B$ composition of LPC tourmaline and hambergite.

5.6. Source of heavy boron of the ESC pegmatite

The ESC pegmatite is a special case because it is situated outside its source pluton and hosted by hornfels of the same protolith as the LPC country rock. However, the major difference between the two localities is that all LPC pegmatites are situated within their source pluton (Fig. 2). Tourmaline and other B-bearing minerals from the ESC pegmatite only occur in a limited section of the pegmatite and form a unique variety of modally abundant B- and Be- minerals such as phenakite Be_2SiO_4, danalite $Be_3Fe_4(SiO_4)_3S$, danburite $CaB_2(SiO_4)_2$ and accessory nordenskiöldine $CaSn(BO_3)_2$ (Sunde, 2013). Compared to the overall size of the exposed pegmatite, the section containing boron-rich mineral assemblages comprise a small and narrow zone where the pegmatite is between 10 cm and 20 cm thick. This zone of the pegmatite consists of major-element minerals that are different relative to the rest of the pegmatite. Particularly Ca and S form the modally abundant minerals described above, whereas the more primitive section consist of sodic pyroxenes and amphiboles. Tourmaline only occurs in this section of the pegmatite, and tourmaline T11 has the highest $\delta^{11}B$ value of all tourmalines analysed in this study, well beyond the range of LPC samples. Spatially the pegmatite is situated in close proximity to the ESC intrusive and within the thermal aureole of feldspar-cordierite hornfels facies. Following the argument for the LPC pegmatites above, it is very likely that the heavy boron ratios of tourmaline T11 reflect external boron derived from metamorphic fluids.

6. Conclusions

From this study of boron isotope ratios of tourmaline and hambergite from silica-saturated and under-saturated rocks, we emphasise the following main findings:

The boron isotopic composition of tourmaline and hambergite show consistently different $\delta^{11}B$ values in samples from peraluminous pegmatites (−13 to −1‰) and those from peralkaline (peralkaline and nepheline syenite) pegmatites (−2 to 12‰). Boron isotope fractionation is consistent between the two minerals, whereby hambergite has heavier/higher $\delta^{11}B$ values (3‰–5‰) relative to tourmaline. This suggests that isotopic equilibrium is approached, and the different $^{11}B/^{10}B$ ratios between tourmaline and hambergite are related to the shorter B—O distances in hambergite. The consistent behaviour of the two minerals in terms of B-isotopes relative to their geological setting suggests that hambergite can be utilized for B-isotope studies. Furthermore, tourmaline is relatively rare in alkaline rocks and does not form from high-pH fluids, whereas hambergite has no such restrictions (although it requires high Be activity). Therefore hambergite is a suitable boron host for boron isotope studies of alkaline rocks. Our results show the importance of using matrix-matched SIMS reference materials for hambergite analyses, and we have developed a new hambergite reference material which is housed at GFZ Potsdam.

The heavy boron isotopic composition of tourmaline and hambergite from the LPC and ESC pegmatites are best explained by externally sourced boron. We attribute this external source to metamorphic fluids derived from thermal metamorphism of the country rock.

Declaration of Competing Interest

None.

Acknowledgement

Svein A. Berge, Peter Andresen, and Alf O. Larsen are thanked for donated LPC samples used in this study. Frédéric Couffignal is thanked for tuning and optimising our SIMS analyses at GFZ, Muriel Erambert for optimising EPMA analyses in Oslo. Two anonymous reviewers are thanked for very constructive and helpful reviews that improved the quality of the manuscript. This study was funded by a Ph.D. stipend to the first author from the Natural History Museum of Oslo, University of Oslo, Norway.

References

Andersen, T., Erambert, M., Larsen, A.O., Selbekk, R.S., 2010. Petrology of nepheline syenite pegmatites in the Oslo Rift, Norway: Zirconium silicate mineral assemblages as indicators of alkalinity and volatile fugacity in mildly agpaitic magma. J. Petrol. 51, 2303–2325.

Andersen, T., Erambert, M., Larsen, A.O., Selbekk, R.S., 2013. Petrology of nepheline syenite pegmatites in the Oslo Rift, Norway: Zr and Ti mineral assemblages in miaskitic and agpaitic pegmatites in the Larvik Plutonic Complex. Mineralogia 44, 61–98.

Bailey, J.C., 2006. Geochemistry of boron in the Ilímaussaq alkaline complex, South Greenland. Lithos 91, 319–330.

Balan, E., Noireaux, J., Mavromatis, V., Saldi, G.D., Montouillout, V., Blanchard, M., Pietrucci, F., Gervais, C., Rustad, J.R., Schott, J., Gaillardet, J., 2018. Theoretical isotopic fractionation between structural boron in carbonates and aqueous boric acid and borate ion. Geochim. Cosmochim. Acta 222, 117–129. https://doi.org/10.1016/j.gca.2017.10.017.

Bosi, F., 2018. Tourmaline crystal chemistry. Am. Mineral. 103, 298–306. https://doi.org/10.2138/am-2018-6289.

Brøgger, W.C., 1890. Die mineralien der syenitpegmatitgänge der Südnorwegischen augit- und nephelinesyenite. Z. Krystallogr. Mineral. 16, 1–663.

Catanzaro, E.J., Champion, C.E., Garner, E.L., Marinenko, G., Sappenfield, K.M., Shields, W.R., 1970. Boric Acid: Isotopic and Assay Standard Reference Materials. National Bureau of Standards (US) Special Publication, pp. 17–260 (70 pp).

Çimen, O., Kuebler, C., Monaco, B., Simonetti, S.S., Corcoran, L., Chen, W., Simonetti, A., 2018. Boron, carbon, oxygen and radiogenic isotope investigation of carbonatite from the Miaoya complex, central China: evidences for late-stage REE hydrothermal event and mantle source heterogeneity. Lithos 322, 225–237. https://doi.org/10.1016/j.lithos.2018.10.018.

Clark, C.M., 2007. Tourmaline: structural formula calculations. Can. Mineral. 45, 229–237.

Dufour, M.S., Kol'tsov, A.B., Zolotarev, A.A., Kuznetsov, A.B., 2007. Corundum-bearing metasomatic rocks in the Central Pamirs. Petrology 15, 160–177. https://doi.org/10.1134/S0869591107020038.

Fisher, J., Foord, E.E., Bricker, G.A., 1998. The geology, mineralogy, and history of the Himalaya Mine, Mesa Grande, San Diego County, California. Rocks Mineral 73, 156–180.

Foster, G.L., Pogge von Strandmann, P.A.E., Rae, J.W.B., 2010. Boron and magnesium isotopic composition of seawater. Geochem. Geophys. Geosyst. 11. https://doi.org/10.1029/2010GC003201 Q08015.

Friis, H., Casey, W.H., 2018. Niobium is highly mobile as a polyoxometalate ion during natural weathering. Can. Mineral. 56, 905–912. https://doi.org/10.3749/canmin.1800058.

Gatta, D.G., McIntyre, G.J., Bromiley, G., Guastoni, A., Nestola, F., 2012. A single-crystal neutron diffraction study of hambergite, $Be_2BO_3(OH,F)$. Am. Mineral. 97, 1891–1897.

Geisinger, K.L., Oestrike, R., Navrotsky, A., Turner, G.L., Kirkpatrick, R.J., 1988. Thermochemistry and structure of glasses along the join $NaAlSi_3O_8$-$NaBSiO_8$. Geochim. Cosmochim. Acta 52, 2405–2414.

Hålenius, U., Skogby, H., Edén, M., Nazzareni, S., Kristiansson, P., Resmark, J., 2010. Coordination of boron in nominally boron-free rock forming silicates: evidence for incorporation of BO_3 groups in clinopyroxene. Geochim. Cosmochim. Acta 74, 5672–5679.

Hansteen, T.H., Burke, E.A.J., 1995. Melt-mineral-fluid interaction in peralkaline silicic intrusions in the Oslo rift, Southeast Norway. II. High-temperature fluid inclusions in the Eikeren-Skrim complex. Nor. Geol. Surv. Bull. 417, 15–32.

Henry, D.J., Novák, M., Hawthorne, F.C., Ertl, A., Dutrow, B.L., Uher, P., Pezzotta, F., 2011. Nomenclature of the tourmaline-supergroup minerals. Am. Mineral. 96, 895–913.

Hervig, R.L., Moore, G.M., Williams, L.B., Peacock, S.M., Holloway, J.R., Roggensack, K., 2002. Isotopic and elemental partitioning of boron between hydrous fluid and silicate melt. Am. Mineral. 87, 769–774.

Hofmeister, M.A., Rossman, R.G., 1985. A spectroscopic study of irradiation coloring of amazonite: structurally hydrous, Pb-bearing feldspar. Am. Mineral. 70, 795–804.

Jamtveit, B., Bucher-Nurminen, K., Stijfhoorn, D.E., 1991. Contact metamorphism of layered shale-carbonate sequences in the Oslo Rift: I. Buffering, infiltration, and the mechanisms of mass transport. J. Petrol. 33, 377–422.

Jamtveit, B., Dahlgren, S., Austrheim, H., 1997. High-grade contact metamorphism of calcareous rocks from the Oslo Rift, Southern Norway. Am. Mineral. 82, 1241–1254.

Kaliwoda, M., Marschall, H.R., Marks, M.A.W., Ludwig, T., Altherr, R., Markl, G., 2011. Boron and boron isotope systematics in the peralkaline Ilímaussaq intrusion (South Greenland) and its granitic country rocks: a record of magmatic and hydrothermal processes. Lithos 125, 51–64.

Kazmi, A.H., Peters, J.J., Obodda, H.P., 1985. Gem pegmatites of the Shingus-Dusso area, Gilgit, Pakistan. Mineral. Rec. 16, 393–411.

Khomyakov, A.P., 1995. Mineralogy of Hyperagpaitic Alkaline Rocks. Oxford University Press, Oxford New York, p. 223.

Kirkpatrick, J.R., Smith, K.A., Schramm, S., Turner, G., Yang, W.-H., 1985. Solid-state nuclear magnetic resonance spectroscopy of minerals. Annu. Rev. Earth Planet. Sci. 13, 29–47.

Kolitsch, U., Andresen, P., Andersen Husdal, T., Ertl, A., Haugen, A., Ellingsen, H.V., Larsen, A.O., 2013. Tourmaline-group minerals from Norway, part II: occurrences of luinaite-(OH) in Tvedalen, Larvik and Porsgrunn, and fluor-liddicoatite, fluor-elbaite and fluor-schorl at Ågskardet, Nordland. Bergverksmuseums Skr. 50, 23–41.

Kowalski, P.M., Wunder, B., 2018. Boron isotope fractionation among vapor-liquids-solids-melts: experiments and atomistic modeling. In: Marschall, H., Foster, G. (Eds.), Boron Isotopes, Advances in Isotope Geochemistry. Springer International Publishing AG 2018, pp. 33–69. https://doi.org/10.1007/978-3-319-64666-4_3.

Kutzschbach, M., Wunder, B., Trumbull, R.B., Rocholl, A., Meixner, A., Heinrich, W., 2017. An experimental approach to quantify the effect of tetrahedral boron in tourmaline on the boron isotope fractionation between tourmaline and fluid. Am. Mineral. 102, 2505–2511. https://doi.org/10.2138/am-2017-6127.

Larsen, A.O., 2010. The Langesundsfjord. History, Geology, Pegmatites, Minerals. Bode, Salzhemmendorf.

Larsen, B.T., Olaussen, S., Sundvoll, B., Heeremans, M., 2008. The Permo-Carboniferous Oslo Rift through six stages and 65 million years. Episodes 31, 52–58.

Laurs, B.M., Dilles, J.H., Snee, L.W., 1996. Emerald mineralization and metasomatism of amphibolite, Khaltaro granitic pegmatite – hydrothermal vein system, Haramosh Mountains, Northern Pakistan. Can. Mineral. 34, 1253–1286.

Laurs, B.M., Dilles, J.H., Wairrach, Y., Kausar, A.B., Snee, L.W., 1998. Geological setting and petrogenesis of symmetrically zoned, miarolitic granitic pegmatites at Stak Nala, Nanga Parbat-Haramosh massif, Northern Pakistan. Can. Mineral. 36, 1–47.

Leeman, W.P., Tonarini, S., 2001. Boron isotopic analysis of proposed borosilicate mineral reference samples. Geostand. Newslett. 25, 399–403.

Liou, J.G., 1971. Analcime equilibria. Lithos 4, 389–402.

Liou, J.G., de Capitani, C., Frey, M., 1991. Zeolite equilibria in the system CaAl2Si2O8 – NaAlSi3O8 – SiO2 – H2O. N. Z. J. Geol. Geophys. 34, 293–301. https://doi.org/10.1080/00288306.1991.9514467.

London, D., 2011. Experimental synthesis and stability of tourmaline: a historical overview. Can. Mineral. 49, 117–136. https://doi.org/10.3749/canmin.49.1.117.

Lussier, A.J., Aguiar, P.M., Michaelis, V.K., Kroeker, S., Hawthorne, F.C., 2009. The occurrence of tetrahedrally coordinated Al and B in tourmaline: an ^{11}B and ^{27}Al MAS NMR study. Am. Mineral. 94, 785–792. https://doi.org/10.2138/am.2009.3000.

Lutro, O., Nordgulen, Ø., 2008. Oslofeltet, berggrunnskart M 1:250 000. Norwegian Geological Survey.

Maner, J.L., London, D., 2017. The boron isotopic evolution of the Little three pegmatites, Ramona, CA. Chem. Geol. 460, 70–83. https://doi.org/10.1016/j.chemgeo.2017.04.016.

Maner, J.L., London, D., 2018. Fractionation of the isotopes of boron between granitic melt and aqueous solution at 700°C and 800°C (200 MPa). Chem. Geol. 489, 16–27. https://doi.org/10.1016/j.chemgeo.2018.05.007.

Markl, G., Baumgartner, L., 2002. pH changes in peralkaline late-magmatic fluids. Contrib. Mineral. Petrol. 144, 331–346.

Marschall, H.R., 2018. Boron isotopes in the ocean floor realm and the mantle. In: Marschall, H., Foster, G. (Eds.), Boron Isotopes, Advances in Isotope Geochemistry. Springer International Publishing AG 2018, pp. 189–215. https://doi.org/10.1007/978-3-319-64666-4_8.

Marschall, H.R., Jiang, S.-Y., 2011. Tourmaline Isotopes: no element left behind. Elements 7, 313–319. https://doi.org/10.2113/gselements.7.5.313.

Marschall, H.R., Meyer, C., Wunder, B., Ludwig, T., Heinrich, W., 2009. Experimental boron isotope fractionation between tourmaline and fluid: confirmation from in situ analyses by secondary ion mass spectrometry and from Rayleigh fractionation modelling. Contrib. Mineral. Petrol. 158, 675–681.

Meyer, C., Wunder, B., Meixner, A., Romer, R.L., Heinrich, W., 2008. Boron-isotope fractionation between tourmaline and fluid: an experimental re-investigation. Contrib. Mineral. Petrol. 156, 259–267.

Morgan, G.B., London, D., 1989. Experimental reactions of amphibolite with boron-bearing aqueous fluids at 200 MPa: implications for tourmaline stability and partial melting in mafic rocks. Contrib. Mineral. Petrol. 102, 281–297.

Neumann, E.-R., 1980. Petrogenesis of the Oslo region larvikites and associated rocks. J. Petrol. 21, 499–531.

Neumann, E.-R., Tilton, G.R., Tuen, E., 1988. Sr, Nd and Pb isotope geochemistry of the Oslo rift igneous province, southeast Norway. Geochim. Cosmochim. Acta 52, 1997–2007.

Neumann, E.-R., Wilson, M., Heeremans, M., Spencer, E.A., Obst, K., Timmerman, M.J., Kirstein, L., 2004. Carboniferous-Permian rifting and magmatism in southern Scandinavia, the North Sea and northern Germany: a review. Geol. Soc. Lond. Spec. Publ. 223, 11–40. https://doi.org/10.1144/GSL.SP.2004.223.01.02.

Oftedal, I., 1964. On the occurrence and distribution of boron in pegmatite. Nor. J. Geol. 44, 217–225.

Pashkov, B.R., Dmitriyev, E.A., 1982. Muzkol' crystalline massif (Central Pamir). Int. Geol. Rev. 24, 285–296.

Peretyazhko, I.S., Zagorsky, V.Y., Smirnov, S.Z., Mikhailov, M.Y., 2004. Conditions of pocket formation in the Oktyabrskaya tourmaline-rich gem pegmatite (the Malkhan field, Central Transbaikalia, Russia). Chem. Geol. 210, 91–111. https://doi.org/10.1016/j.chemgeo.2004.06.005.

Petersen, J.S., 1978. Structure of the larvikite-lardalite complex, Oslo-region, Norway, and its evolution. Geol. Rundsch. 67, 330–342.

Pezzotta, F., Dini, A., Tonarini, S., 2010. Three- and four-coordinated boron minerals in pegmatites hosted in dolomitic marble in Central Madagascar; paragenesis and boron isotopes. Acta Mineralogica-Petrographica Abstract Series (IMA 2010). Vol. 6, p. 474.

Piilonen, P.C., McDonald, A.M., Poirier, G., Rowe, R., Larsen, A.O., 2013. Mafic minerals of the alkaline pegmatites in the Larvik Plutonic Complex, Oslo rift, Southern Norway. Can. Mineral. 51, 735–770.

Pouchou, J.L., Pichoir, F., 1984. A new model for quantitative X-ray microanalysis. I. Application to the analysis of homogenous samples. Rech. Aèrospat. 3, 13–38.

Raade, G., Åmli, R., Mladeck, M.H., Din, V.K., Larsen, A.O., Åsheim, A., 1983. Chiavennite from syenite pegmatites in the Oslo region, Norway. Am. Mineral. 68, 628–633.

Rämo, O.T., Andersen, T., 2011. Magmatic evolution of the Permo-Carboniferous Oslo rift: U-Pb- and Lu-Hf-in-zircon evidence from the 299–289 Ma Larvik plutonic complex. Abstract V12B-02 Presented at the 2011 Fall Meeting, AGU, San Francisco, CA, 2–9. December.

Rasmussen, E., Neumann, E.-R., Andersen, T., Sundvoll, B., Fjerdingstad, V., Stabel, A., 1988. Petrogenetic processes associated with intermediate and silicic magmatism in the Oslo rift, south-east Norway. Mineral. Mag. 52, 293–307.

Schmidt, C., Thomas, R., Heinrich, W., 2005. Boron speciation in aqueous fluids at 22 to 600°C and 0.1 MPa to 2 GPa. Geochim. Cosmochim. Acta 69, 275–281.

Shannon, R.D., 1976. Revised effective ionic radii and systematic studies of interatomic distances in halides and chalcogenides. Acta Crystallogr. 32, 751–767.

Sheldrick, G.M., 2008. A short history of SHELX. Acta Crystallogr. A64, 112–122.

Sheldrick, G.M., 2015. Crystal structure refinement with SHELXL. Acta Crystallogr. C71, 3–8.

Siegel, K., Wagner, T., Trumbull, R.B., Jonsson, E., Matalin, G., Wälle, M., Heinrich, C.A., 2016. Stable isotope (B, H, O) and mineral-chemistry constraints on the magmatic to hydrothermal evolution of the Varuträsk rare-element pegmatite (Northern Sweden). Chem. Geol. 421, 1–16. https://doi.org/10.1016/j.chemgeo.2015.11.025.

Sunde, Ø., 2013. Mineralogy and Petrology of the Amazonite Pegmatite at Bakstevalåsen, øvre Eiker. Master thesis. Department of Geosciences, University of Oslo.

Sunde, Ø., Friis, H., Andersen, T., 2018. Variation in major and trace elements of primary wöhlerite as an indicator of the origin of pegmatites in the Larvik Plutonic Complex, Norway. Can. Mineral. 56, 529–542. https://doi.org/10.3749/canmin.1700050.

Sunde, Ø., Friis, H., Andersen, T., 2019. Pegmatites of the Larvik Plutonic Complex, Oslo Rift, Norway: Field relations and characterisation. Nor. J. Geol. 99, 1–20. https://doi.org/10.17850/njg99-1-05.

Sundvoll, B., Neumann, E.-R., Larsen, B.T., Tuen, E., 1990. Age relations among Oslo Rift magmatic rocks: implications for tectonic and magmatic modelling. Tectonophysics 178, 67–87.

Thomas, R., Davidson, P., 2010. Hambergite-rich melt inclusions in morganite crystals from the Muiane pegmatite, Mozambique and some remarks on the paragenesis of hambergite. Mineral. Petrol. 100, 227–239.

Thomas, R., Davidson, P., Badanina, E., 2012. Water- and boron-rich melt inclusions in quartz from the Malkhan pegmatite, Transbaikalia, Russia. Minerals 2, 435–458. https://doi.org/10.3390/min2040435.

Tonarini, S., Pennisi, M., Leeman, W.P., 1997. Precise boron isotopic analysis of complex silicate (rock) samples using alkali carbonate fusion and ion-exchange separation. Chem. Geol. 142, 129–137.

Tonarini, S., Forte, C., Petrini, R., Ferrara, G., 2003. Melt/biotite $^{11}B/^{10}B$ isotopic fractionation and the boron local environment in the structure of volcanic glasses. Geochim. Cosmochim. Acta 67, 1863–1873.

Trumbull, R.B., Slack, J.F., 2018. Boron isotopes in the continental crust: granites, pegmatites, felsic volcanic rocks, and related ore deposits. In: Marschall, H., Foster, G. (Eds.), Boron Isotopes, Advances in Isotope Geochemistry. Springer International Publishing AG 2018, pp. 249–272. https://doi.org/10.1007/978-3-319-64666-4_10.

Trumbull, R.B., Beurlen, H., Wiedenbeck, M., Soares, D.R., 2013. The diversity of B-isotope variations in tourmaline from rare-element pegmatites in the Borborema Province of Brazil. Chem. Geol. 352, 47–62. https://doi.org/10.1016/j.chemgeo.2013.05.021.

Turner, G.L., Smith, K.A., Kirkpatrick, J.R., Oldfield, E., 1986. Boron-11 nuclear magnetic resonance spectroscopic study of borate and borosilicate minerals and a borosilicate glass. J. Magn. Reson. 67, 544–550.

Van Hinsberg, V.J., Henry, D.J., Marschall, H.R., 2011. Tourmaline: an ideal indicator of its host environment. Can. Mineral. 49, 1–16. https://doi.org/10.3749/canmin.49.1.1.

Vladykin, N.V., Sotnikova, I.A., 2017. Petrology, geochemistry and source characteristics of the Burpala alkaline massif, North Baikal. Geosci. Front. 8, 711–719.

Vorbach, A., 1989. Experimental examinations on the stability of synthetic tourmalines in temperatures from 250°C to 750°C and pressures up to 4 kb. N. Jb. Mineral. Abh. 161, 69–83.

Wolf, M.B., London, D., 1997. Boron in granitic magmas: Stability of tourmaline in equilibrium with biotite and cordierite. Contrib. Mineral. Petrol. 130, 12–30.

Wu, J., Stebbins, J.F., 2009. Effects of cation field strength on the structure of aluminoborosilicate glasses: high-resolution 11B, 27Al and 23Na MAS NMR. J. Non-Cryst. Solids 355, 556–562. https://doi.org/10.1016/j.jnoncrysol.2009.01.025.

Wu, J., Stebbins, J.F., 2013. Temperature and modifier cation field strength effects on aluminoborosilicate glass network structure. J. Non-Cryst. Solids 362, 73–81. https://doi.org/10.1016/j.jnoncrysol.2012.11.005.

Wunder, B., Meixner, A., Romer, R.L., Wirth, R., Heinrich, W., 2005. The geochemical cycle of boron: constraints from boron isotope partitioning experiments between mica and fluid. Lithos 84, 206–216.

Zagorsky, V.Ye., 2015. Sosedka pegmatite body at the Malkhan Deposit of gem tourmaline, Transbaikalia: composition, inner structure, and petrogenesis. Petrologiya 23, 75–100. https://doi.org/10.1134/S0869591115010075.

Zagorsky, V.E., Peretyazhko, I.S., 2010. First $^{40}Ar/^{39}Ar$ age determinations of the Malkhan granite-pegmatite system: geodynamic implications. Dokl. Earth Sci. 430, 172–175. https://doi.org/10.1134/S1028334X10020054.